Monthly Notices of the ROYAL ASTRONOMICAL SOCIETY

MNRAS **504,** 4907–4922 (2021)
Advance Access publication 2021 April 13

doi:10.1093/mnras/stab1009

The double-peaked Type Ic supernova 2019cad: another SN 2005bf-like object

C. P. Gutiérrez [1,2,3★] M. C. Bersten,[4,5,6] M. Orellana,[7,8] A. Pastorello,[9] K. Ertini,[4,5] G. Folatelli,[4,5,6] G. Pignata,[10,11] J. P. Anderson,[12,11] S. Smartt,[13] M. Sullivan [3] M. Pursiainen [3,14] C. Inserra [15] N. Elias-Rosa,[9,16] M. Fraser [17] E. Kankare,[2] S. Moran,[2] A. Reguitti,[10,11,9] T. M. Reynolds,[2] M. Stritzinger,[18] J. Burke,[19,20] C. Frohmaier [21] L. Galbany [22] D. Hiramatsu,[19,20] D. A. Howell,[19,20] H. Kuncarayakti,[1,2] S. Mattila,[2] T. Müller-Bravo [3] C. Pellegrino[19,20] and M. Smith [23]

Affiliations are listed at the end of the paper

Accepted 2021 April 6. Received 2021 April 6; in original form 2021 February 6

ABSTRACT

We present the photometric and spectroscopic evolution of supernova (SN) 2019cad during the first ∼100 d from explosion. Based on the light-curve morphology, we find that SN 2019cad resembles the double-peaked Type Ib/c SN 2005bf and the Type Ic PTF11mnb. Unlike those two objects, SN 2019cad also shows the initial peak in the redder bands. Inspection of the *g*-band light curve indicates the initial peak is reached in ∼8 d, while the *r*-band peak occurred ∼15 d post-explosion. A second and more prominent peak is reached in all bands at ∼45 d past explosion, followed by a fast decline from ∼60 d. During the first 30 d, the spectra of SN 2019cad show the typical features of a Type Ic SN, however, after 40 d, a blue continuum with prominent lines of Si II λ6355 and C II λ6580 is observed again. Comparing the bolometric light curve to hydrodynamical models, we find that SN 2019cad is consistent with a pre-SN mass of 11 $M_\odot$, and an explosion energy of 3.5×10^{51} erg. The light-curve morphology can be reproduced either by a double-peaked ^{56}Ni distribution with an external component of 0.041 $M_\odot$, and an internal component of 0.3 $M_\odot$ or a double-peaked ^{56}Ni distribution plus magnetar model ($P \sim 11$ ms and $B \sim 26 \times 10^{14}$ G). If SN 2019cad were to suffer from significant host reddening (which cannot be ruled out), the ^{56}Ni model would require extreme values, while the magnetar model would still be feasible.

Key words: supernovae: general – supernovae: individual: SN 2019cad.

1 INTRODUCTION

Core-collapse supernovae (SNe) are produced by the explosion of massive stars ($M_{ZAMS} > 8$–$10\ M_\odot$). They are traditionally classified into different classes depending on the presence or absence of certain lines. SNe from collapsing stars that do not show hydrogen but show helium in their spectra are classified as Type Ib SNe (SNe Ib), while those with no hydrogen or helium are classified as Ic SNe (SNe Ic; e.g. Filippenko 1997; Gal-Yam 2017; Modjaz, Gutiérrez & Arcavi 2019). The absence of these spectral lines implies their progenitor stars shed their hydrogen- and helium-rich envelops over their lifetimes, mainly due to strong stellar winds (Heger et al. 2003; Georgy et al. 2009) or binary interaction (e.g. Podsiadlowski, Joss & Hsu 1992; Nomoto, Iwamoto & Suzuki 1995; Eldridge, Izzard & Tout 2008). While both mechanisms are successful in explaining the absence of the hydrogen layer, removing the helium layer is still a challenge as it is found in denser parts of the star. Given these complications, it has been proposed that some helium is possibly present in SNe Ic but it is not seen in the spectrum because it is not excited (Dessart et al. 2012, but see Williamson, Kerzendorf & Modjaz 2021). On the other hand, recent observational evidence, such as the low progenitor masses inferred for SNe Ic from their light curves (Drout et al. 2011; Lyman et al. 2016; Taddia et al. 2018b) and the relative SN Ic rate (Smith et al. 2011), favours the binary scenario.

The direct identification of stars in pre-explosion images can give more insights about the nature of the SN progenitor (e.g. Van Dyk et al. 2002; Van Dyk, Li & Filippenko 2003; Mattila et al. 2008; Smartt et al. 2009; Van Dyk 2017). However, for hydrogen-free objects only a couple of cases exist: a confirmed progenitor for the SN Ib iPFT13bvn (Cao et al. 2013; Folatelli et al. 2016) and two progenitor candidates, one for the Type Ic SN 2017ein (Kilpatrick et al. 2018; Van Dyk et al. 2018; Xiang et al. 2019) and another one for the Type Ib SN 2019yvr (Kilpatrick et al. 2021). If post-explosion images confirm the progenitor association, then it would represent the first progenitor detection for an SN Ic and the second for an SN Ib.

SNe Ic are the most intriguing objects among core-collapse events. They represent a heterogeneous class showing a large range in luminosity and light-curve shapes (e.g. Bianco et al. 2014; Lyman et al. 2016; Prentice et al. 2016; Taddia et al. 2018b), as well as diverse spectra (e.g. Matheson et al. 2001; Modjaz et al. 2014; Shivvers et al. 2019). A small fraction of SNe Ic have been observed with broad absorption lines that have been associated with long-duration gamma-ray bursts (GRBs; Woosley & Bloom 2006; Cano et al. 2017). These objects, usually labelled as broad-line SNe Ic (SNe Ic-

★ E-mail: claudia.gutierrez@utu.fi

BL), represent a challenge in our understanding of the explosion mechanism and final steps of massive-star evolution. Fortunately, high-cadence surveys are detecting and following up more objects of this type allowing their characterization and physical understanding.

Stripped-envelope SNe, considered as hydrogen-deficient objects, usually present bell-shaped light curves, with a single peak reached a couple of weeks after explosion. These light curves are powered by the decay of ^{56}Ni to ^{56}Co, and then to ^{56}Fe. Some stripped-envelope SNe with a well-constrained explosion date and good photometric cadence have shown early emission prior to the usual nickel peak. When it is observed, this initial peak lasts a few days and has been attributed to the cooling of the ejecta after the shock breakout (e.g. Woosley et al. 1994; Bersten et al. 2012; Nakar & Piro 2014), while the second peak has a duration of a couple of weeks and is mainly powered by the decay of ^{56}Ni. There are now many cases where the SN was observed before the nickel peak (see Modjaz et al. 2019, and references therein), but most of them were classified as SN IIb (transitional objects between SNe II and SNe Ib) and the emission can be well explained as due to the cooling of a thin but extended hydrogen envelope. In the other known cases, they showed some peculiarities, as was the case of the Type Ib SN 2008D associated with an X-ray flash (Mazzali et al. 2008; Soderberg et al. 2008), or the cases of the SNe Ic SN 2006aj (Campana et al. 2006) and more recently SN 2017iuk (Izzo et al. 2019) associated with long-duration GRBs (i.e. SN Ic-BL). In these cases, the early emission is harder to explain due to the cooling of an envelope and because of the compact nature of their progenitor. Some alternatives, such as the presence of circumstellar material, the cooling of a cocoon jet or some external nickel seem to be required (Soderberg et al. 2008; Bersten et al. 2013).

Unlike the early emission discussed above, which lasts for a few days, there are two objects in the literature where the early emission is longer in duration, appearing as a peak at around 20 d from the explosion, followed by a main peak occurring at ∼40 d from the explosion. These objects are SN 2005bf (Anupama et al. 2005; Tominaga et al. 2005; Folatelli et al. 2006) and PTF11mnb (Taddia et al. 2018a). SN 2005bf was classified as a transitional object between SNe Ic and SNe Ib (Folatelli et al. 2006), while PTF11mnb was catalogued as a typical SN Ic. Anupama et al. (2005) claimed that SN 2005bf was the explosion of a massive He star with some H left. Tominaga et al. (2005) concluded that the progenitor was a Wolf–Rayet WN star and the morphology of the light curve can be reproduced by a double-peaked ^{56}Ni distribution. Folatelli et al. (2006) found that the most favoured model is consistent with an energetic and asymmetric explosion of a massive WN star, where an unobserved relativistic jet was launched producing a two-component explosion. Finally, through analysing late-phase spectroscopy and photometry of SN 2005bf, Maeda et al. (2007) suggested that the power source of this SN is a magnetar. On the other hand, for PTF11mnb, Taddia et al. (2018a) suggested that the progenitor was a massive single star with a double-peaked ^{56}Ni distribution powering the SN light curve.

In this paper, we present photometry and spectra of a peculiar event, the Type Ic SN 2019cad. We discuss its observed properties and compare it with SN 2005bf and PTF11mnb. The paper is organized as follows. A description of the observations and data reduction are presented in Section 2. In Section 3, we describe the photometric and spectral properties of SN 2019cad and a comparison with similar events. The progenitor properties are analysed through hydrodynamic modelling in Section 4, while in Section 5 we present the discussion and conclusions. Throughout, we assume a flat ΛCDM universe, with a Hubble constant of $H_0 = 70\,\mathrm{km\,s^{-1}\,Mpc^{-1}}$, and $\Omega_\mathrm{m} = 0.3$.

2 OBSERVATIONS OF SN 2019CAD

SN 2019cad (also known as ZTF19aamsetj and ATLAS19ecc) was discovered by the Zwicky Transient Facility (ZTF; Bellm et al. 2019; Graham et al. 2019) on 2019 March 17 (MJD = 58559.24) at a magnitude of $m_r = 19.02 \pm 0.11$ mag (Nordin et al. 2019). The last non-detection obtained by ZTF occurred on 2019 March 16 (MJD = 58558.19) with a detection limit of $m_r \sim 19.183$ mag. A deeper early detection and a non-detection were obtained by the Asteroid Terrestrial-impact Last Alert System (ATLAS; Tonry et al. 2018; Smith et al. 2020) on 2019 March 12 (MJD = 58554.42; $m_o = 19.91 \pm 0.11$ mag) and 2019 March 4 (MJD = 58546.46; $m_o = 20.50$ mag), respectively. These new constraints allow us to adopt the mid-point between the last non-detection and first detection as the explosion epoch (MJD = 58550.44 ± 4 (2019 March 8).

On 2019 March 22 (MJD = 58564.36), SN 2019cad was observed spectroscopically by the Global SN Project (GSP) and classified as an SN Ic around maximum light at a redshift $z = 0.0267$ (Burke et al. 2019). In the classification report, Burke et al. (2019) noted the object was slightly faint (i.e. $M_r \sim -16.6$ mag) compared what is typically observed in SNe Ic. 20 d after the classification, the *r*-band ZTF light curve showed a rebrightening, which was confirmed 5 d later in the *g* band. Because of this rebrightening, we started a follow-up campaign the details of which are now described.

2.1 Photometry

Photometric coverage of SN 2019cad was acquired using different facilities and instruments over a period of 14 weeks as follows:

(i) **ATLAS:** Photometry in the orange (*o*) filter (a red filter that covers a wavelength range of 5600 to 8200 Å) and cyan (*c*) filter (wavelength range 4200 to 6500 Å) was obtained by the twin 0.5 m ATLAS telescope system (Tonry et al. 2018), spanning from 2019 March 11 to 2019 May 30. The data were reduced and calibrated automatically as described in Tonry et al. (2018) and Smith et al. (2020). Table A1 lists the mean magnitudes.

(ii) **Gran Telescopio Canarias:** One epoch of *r*-band photometry was obtained with the 10.4-m Gran Telescopio Canarias (GTC) using OSIRIS. The *r*-image was reduced with IRAF following standard procedures. The photometry was performed using the PYTHON package PHOTUTILS (Bradley et al. 2019) of ASTROPY (Astropy Collaboration 2018). The *r* magnitude was calibrated using Pan-STARRS (Chambers et al. 2016; Magnier et al. 2020).

(iii) **Las Cumbres Observatory:** Multiband photometry was obtained with the 1.0-m telescopes of Las Cumbres Observatory (Brown et al. 2013) at three different epochs through the Global Supernova Project (GSP). The data reduction and SN photometry measurements were performed following the prescriptions described in Firth et al. (2015).

(iv) **Liverpool Telescope:** Five epochs of *ugriz* were obtained with the 2-m Liverpool Telescope (LT; Steele et al. 2004) using the IO:O imager. LT data were reduced using the standard IO:O pipeline. The photometry was performed using PHOTUTILS. The *ugriz* magnitudes were calibrated using Pan-STARRS sequences.

(v) **Nordic Optical Telescope:** Using the 2.56-m Nordic Optical Telescope (NOT) at Roque de los Muchachos Observatory, we obtained six epochs of *ugriz* photometry from April 23 to June 19, and three epochs of *JHK* photometry from April 30 to June 13. The optical observations were performed with ALFOSC, and the near-infrared (NIR) observations with NOTCam. All NOT observations were obtained through the NOT Unbiased Transient Survey (NUTS) allocated time. Optical and NIR data reduction and SN photometry

measurements were performed using the PYTHON/PYRAF SNOoPY pipeline (Cappellaro 2014). The *ugriz* magnitudes were calibrated using observations of local Sloan and Pan-STARRS sequences, while the *JHK* magnitudes were calibrated using 2MASS (Skrutskie et al. 2006).

(vi) **Neil Gehrels *Swift* Observatory:** One epoch of UltraViolet (UV) Optical observations were obtained with the UltraViolet/Optical Telescope (UVOT) on board the Swift spacecraft. Imaging observations were processed with aperture photometry following Brown et al. (2009). No template subtractions were achieved.

(vii) **William Herschel Telescope:** One epoch of *gr* photometry was obtained with ACAM in the William Herschel Telescope (WHT) on 2019 June 20. The images were reduced with IRAF following standard procedures, while the photometry was performed using PHOTUTILS. The *gr* magnitudes were calibrated using Pan-STARRS.

Optical, NIR, and UVOT photometry are presented in Tables A2, A3, and A4, respectively. Additional photometry in the *gr* bands was obtained from the ZTF public stream through the Lasair[1] broker (Smith et al. 2019) and presented in Table A5.

2.2 Spectroscopy

SN 2019cad was observed spectroscopically at 12 epochs spanning phases between 13.6 to 88.1 d past explosion. These observations were acquired with five different instruments: ALFOSC at the NOT, SPRAT (Piascik et al. 2014) at the LT, the FLOYDS spectrograph (Brown et al. 2013) on the Faulkes Telescope South (FTS), OSIRIS at the GTC, and with the Spectral Energy Distribution Machine (SEDM; Blagorodnova et al. 2018) on the automated 60-in telescope at Palomar Observatory (P60; Cenko et al. 2006).[2] The log of spectroscopic observations of SN 2019cad is presented in Table A6.

Data reductions for ALFOSC and OSIRIS were performed following standard routines in IRAF. The SPRAT data were reduced using the Fast and Dark Side of Transient experiment Fast extraction pipeline (FDSTfast).[3] FLOYDS spectra were reduced using the PYRAF-based FLOYDS_PIPELINE[4] (Valenti et al. 2014), while the public SEDM spectrum was automatically reduced by the IFU data reduction pipeline (Rigault et al. 2019). All spectra are available via the WISeREP[5] repository (Yaron & Gal-Yam 2012).

3 CHARACTERIZING SN 2019CAD

3.1 Host galaxy

The host galaxy of SN 2019cad was identified as UGC 4798, a spiral galaxy at a redshift of 0.0267 (de Vaucouleurs et al. 1991).[6] Adopting the recessional velocity corrected for Local Group infall into Virgo reported by HyperLEDA[7] (Makarov et al. 2014; $v_{\rm vir} = 8152 \pm 3$ km s^{-1}), we obtain a distance modulus $\mu = 35.38 \pm 0.13$ mag, which is equivalent to a distance of 119.2 ± 8.4 Mpc.

SN 2019cad was located 3.″6 east and 7.″6 north from the galaxy centre. Its host has been classified as a H I-rich galaxy (Wang et al. 2013) with a stellar mass of $\log_{10}(M_*) = 10.59\,M_\odot$ (Chen et al. 2012) and a star formation rate (SFR) of $1.97 \pm 0.01\ M_\odot {\rm yr}^{-1}$ (Cormier et al. 2016). SN 2019cad is the fourth SN reported in UGC 4798. SN 2005mf was detected at 5.″9 west and 13.″3 north from the galaxy centre (Bian et al. 2005), SN 2013V was found at 11.″5 west and 11.″1 north of the centre of the galaxy (Crowley et al. 2013), while SNHunt263 was detected at 1.″ west and 25.″ south of the centre of the galaxy (Drake et al. 2009). SN 2005mf was classified as an SN Ic (Modjaz et al. 2005), while SN 2013V and SNHunt263 as SNe Ia (Tomasella et al. 2013; Elias-Rosa et al. 2014). All these SNe have been located at projected distances larger than 4.5 kpc from the centre of the galaxy, see Fig. 1. The substantial number of SNe detected in UGC 4798 in the last 15 yr is not rare. Previous studies (e.g. Thöne et al. 2009; Anderson & Soto 2013) have shown that several galaxies have been hosted multiple SNe. Most of these galaxies have a high SFR. However, for NGC 2770, the high number of SNe Ib was found by Thöne et al. (2009) to be a coincidence.

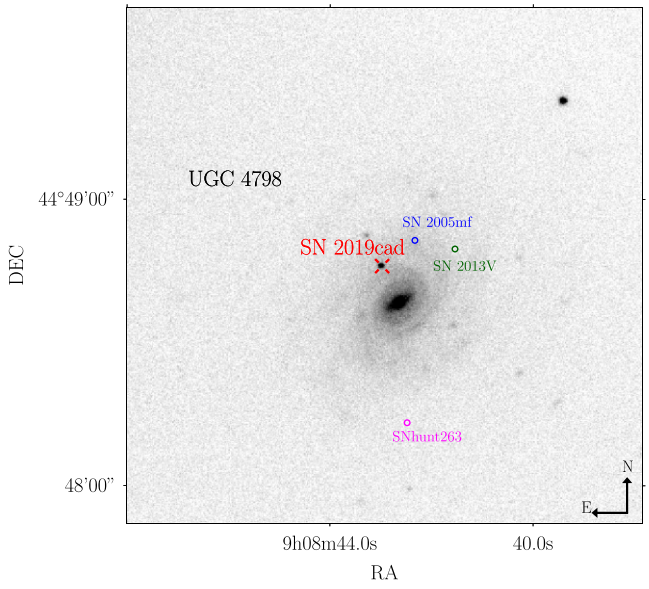

Figure 1. NOT *r*-band image of SN 2019cad and its host galaxy. SN 2019cad is marked with a red crosshair. The locations of SN 2005mf (Ic), SN 2013V (Ia), and SNHunt263 (Ia) are marked in blue, green, and magenta circles, respectively. The orientation of the image is indicated in the bottom-right corner.

To estimate the oxygen abundance of UGC 4798, we use the public spectrum of the central region of the galaxy obtained from the Sloan Digital Sky Survey (SDSS; Ahumada et al. 2020). Applying the O3N2 diagnostic method from Pettini & Pagel (2004), we obtain an oxygen abundance of $12 + \log({\rm O/H}) = 8.72 \pm 0.08$. Employing the same method, Modjaz et al. (2011) reported an oxygen abundance at the position of SN 2005mf of $12 + \log({\rm O/H}) = 8.66 \pm 0.09$, which is around the solar abundance (e.g. Pettini & Pagel 2004). Based on the small differences in these two estimations, we suggest the oxygen abundance near SN 2019cad to be around solar.

3.2 Extinction estimation

To determine the intrinsic properties of SN 2019cad, an estimation of the total reddening (from both the Milky Way and the host galaxy) along the line of sight to the object is needed. The galactic reddening was found to be $E(B-V)_{\rm MW} = 0.015$ mag (Schlafly & Finkbeiner 2011). To calculate the host galaxy extinction, we searched for the

[1] https://lasair.roe.ac.uk/
[2] Public spectrum obtained from the TNS webpage: https://wis-tns.weizmann.ac.il/object/2019cad.
[3] https://github.com/cinserra/FDST
[4] https://github.com/LCOGT/floyds_pipeline
[5] https://wiserep.weizmann.ac.il/
[6] http://ned.ipac.caltech.edu/
[7] http://leda.univ-lyon1.fr

Na I D absorption lines in the SN spectra. A narrow Na I D line at the host galaxy rest wavelength is clearly detected in the NOT spectra, with an equivalent width (EW) of ∼1.32 Å. This strong absorption suggests a significant reddening from the host galaxy. Using the relations of $E(B-V)$ and EW(Na I D) found by Turatto, Benetti & Cappellaro (2003) from low and heavily reddened SNe Ia, we obtain two values: $E(B-V)_{\rm Host} = 0.21$ and 0.63 mag. Applying the empirical relation from Poznanski, Prochaska & Bloom (2012), we find an $E(B-V)_{\rm Host} = 0.49 \pm 0.08$ mag. Unfortunately, there are large discrepancies in these estimations, which is likely caused by the fact that the lines have saturated (Munari & Zwitter 1997; Poznanski et al. 2011). Therefore, we explored alternative methods to determine the host extinction.

Constraints on the host extinction can be also found using the colour of the SN around the maximum (Drout et al. 2011; Taddia et al. 2015; Stritzinger et al. 2018). Drout et al. (2011) found that in SNe Ibc the $V-R$ colour at 10 d from the V-band maximum shows very small scatter, varying between 0.18 and 0.34 mag. Later, Stritzinger et al. (2018), following a similar approach, but using a range of optical or optical/NIR colour combinations, built intrinsic colour-curve templates, which we can use to measure the colour excess. By comparing the SN 2019cad $g-r$ and $r-i$ colours with the templates from Stritzinger et al. (2018), we found an excess in $r-i$ that corresponds to $E(B-V) \sim 0.22$ mag, however, the $g-r$ colours were found to be bluer than the template (see Fig. 2, middle panel). Because of the inconsistency in the colours (excess in $r-i$, but deficit in $g-r$), this method is not applicable in this SN, which could have been expected from its peculiar evolution.

Another method to estimate the host reddening is to derive the Balmer decrement from an H II region that we assume is sharing the same extinction of the SN along the line of sight. In the latest spectrum of SN 2019cad, a weak emission from Hα and Hβ is detectable. To measure the flux of latter emission lines, we remove the SN flux following the procedure presented in Pignata et al. (2011). We stress the fact that due to the very low signal-to-noise ratio of Hβ (∼2.0), the measurement of its flux is very uncertain, therefore we consider its minimum and maximum flux to obtain an estimation of the maximum ($E(B-V) = 0.80$ mag) and minimum ($E(B-V) = 0.28$ mag) colour excess along the line of sight of SN 2019cad. Even though with large uncertainties, such values provide additional evidence that SN 2019cad is highly reddened.

The reddening estimation is one of the largest systematic uncertainties in the SN field. As we have shown above, large differences are found using different methods. The methods used were obtained for normal core-collapse SNe, and even in these cases it is not clear which methods are robust, if any. The situation is even worse for peculiar events as SN 20019cad. Therefore, we decided not to consider host galaxy extinction in the rest of this paper, but we explore in Section 3.7 and Section 5 the implications of a larger host galaxy reddening ($E(B-V)_{\rm Host} = 0.49$ mag, the median of these estimations and the value obtained with the most recent empirical relation of $E(B-V)$ and EW(Na I D)).

3.3 Light curves

The multiband light curves of SN 2019cad are shown in Fig. 2 (top panel). SN 2019cad presents an unusual light-curve evolution characterized by the presence of an initial peak between 10 and 20 d from explosion, followed by the main peak at ∼45 d. This double-peaked light curve resembles those of the peculiar Type Ic SN 2005bf (Folatelli et al. 2006) and PTF11mnb (Taddia et al. 2018a).

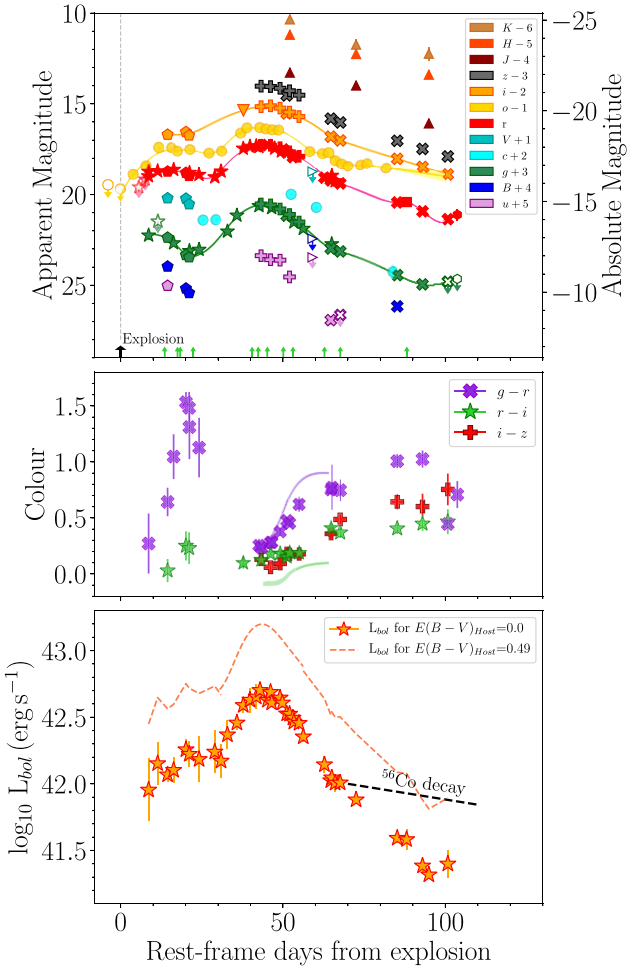

Figure 2. Upper panel: Optical light curves of SN 2019cad. ATLAS photometry is presented as circles, ZTF photometry as stars, NOT photometry as crosses, LT photometry as pluses, Las Cumbres photometry as pentagons, NOTCam photometry as up-facing triangles, GTC photometry as squares, WHT photometry as hexagons, and Swift photometry as right-facing triangles. Upper limits are presented as open symbols. The explosion estimation is indicated as a vertical black arrow. The vertical lime-green arrows represent epochs of optical spectroscopy. The photometry is corrected for Milky Way extinction. The solid lines show the Gaussian process (GP) interpolation. Middle panel: Colour curves of SN 2019cad. Only corrections for Milky Way extinction have been made. Solid lines (purple and green) show the intrinsic colour-curves templates ($g-r$ and $r-i$) from Stritzinger et al. (2018). Bottom panel: Bolometric light curve of SN 2019cad assuming an $E(B-V)_{\rm Host} = 0.0$ mag (stars) and $E(B-V)_{\rm Host} = 0.49$ mag (dashed line).

To estimate the main parameters of the light curves, we use Gaussian processes (GPs). Following Gutiérrez et al. (2020), we perform the light curve interpolation with the PYTHON package GEORGE (Ambikasaran et al. 2015) using the Matern 3/2 kernel. We find that SN 2019cad reaches an initial peak absolute g-band magnitude of $M_g = -16.35$ mag in ∼8 d. In the r and o bands, the initial peak is $M_r = -16.68$ mag and $M_o = -16.86$ mag at ∼15 and ∼18.9 d, respectively. After this peak, the light curves in the o and r bands show a small decrease in brightness (between ∼0.2 and 0.4 mag in ∼10 d), while the g band decreases more than 1 mag in the same period (∼13 d). Following this initial peak, a rise of 1.5–3 mag is observed in all bands. The peak in *groi* occurs at ∼43.9, 44.3, 41.5, and 44.9 d with magnitudes of $M_g^{\rm max} = -17.83$ mag,

Table 1. Light-curve parameters of SN 2019cad assuming an $E(B-V)_{\rm Host}=0$ mag.

Band	Initial peak magnitude (mag)	Epoch (d)	Main peak magnitude (mag)	Epoch (d)	Change in magnitude from the main peak to 20 d post-peak (mag)	Decline rate after 60 d (mag per 100 d)
g	−16.35	8	−17.83	43.9	2.20	7.10 ± 0.21
r	−16.68	15	−18.10	44.3	1.71	5.91 ± 0.25
o	−16.86	18.9	−18.07	41.5	1.50	5.33 ± 1.12
i	–	–	−18.26	44.9	1.67	5.83 ± 0.10

$M_r^{\rm max}=-18.10$ mag, $M_o^{\rm max}=-18.07$ mag, and $M_i^{\rm max}=-18.26$ mag. Once SN 2019cad has reached the main peak, the light curves decrease by 2.20 (*g*), 1.71 (*r*), 1.67 (*i*), 1.50 (*o*), and 1.45 (*z*) mag in ∼20 d. Table 1 shows a summary of the light-curve parameters.

From 60 to 100 d, the light curve shows a linear decline in *griz*. The slope of the decline in all bands is faster than the expected from the full trapping of gamma-ray photons and positrons from the decay of ^{56}Co (0.98 mag per 100 d; Woosley, Hartmann & Pinto 1989). Fitting a line to the tail, we measure a slope of 7.10 ± 0.21 mag $(100{\rm d})^{-1}$ in the *g* band and 5.91 ± 0.25 mag $(100{\rm d})^{-1}$ in the *r* band. To guarantee that we use luminosities when the light curve has entered the nebular phase, we follow the prescriptions of Meza & Anderson (2020) and we fit a line to the tail from 75 to 100 d. Thus, we derive a slope of 6.54 ± 0.31 mag $(100{\rm d})^{-1}$ in *g* and 6.00 ± 0.21 mag $(100{\rm d})^{-1}$ in *r*. Taddia et al. (2018b) found that the linear decay slope for SNe Ic is between 1.7 and 2.7 mag $(100{\rm d})^{-1}$. These declines are faster than the expected from the ^{56}Co decay, but slower than those measured in SN 2019cad. If the radioactive decay powers the light curve, then the extremely fast decline suggests a significant leakage of gamma-ray photons which can, for example, be achieved assuming a low-mass ejecta.

The colour curves of SN 2019cad are presented in the middle panel of Fig. 2. During the first 20 d, SN 2019cad becomes redder, going from a colour of $g-r=0.27$ mag at 8.6 d to $g-r=1.53$ mag at 20.1 d. At around 20 d, the $g-r$ colour shows a maximum that corresponds to the initial peak in the optical light curves. After this peak, the SN evolves to bluer colours, reaching a minimum of $g-r=0.24$ mag at ∼44 d. This $g-r$ minimum matches with the main peak of the light curves. From 43 to 100 d, the SN slowly becomes redder again. A similar but less intense colour evolution is observed in $r-i$ and $i-z$.

3.4 Bolometric luminosity

Using the *groiz* photometry, we build a pseudo-bolometric light curve for SN 2019cad. First, we interpolated the observed magnitudes using GPs to have the *groiz* light curves with similar coverage at the same epochs. Then, extinction-corrected (only galactic extinction) *groiz* magnitudes were converted into fluxes at the effective wavelength of the corresponding filters. Next, we integrated a spectral energy distribution (SED) over the wavelengths covered, assuming zero flux beyond the integration limits. Fluxes were converted to luminosity using the distance adopted in Section 1. To estimate the full bolometric light curve, we extrapolated the SED constructed from the *groiz*. In the UV, we did a linear extrapolation to zero flux at 3000 Å. On the NIR side, the fluxes were extrapolated using a blackbody fit to the SED. This way to extrapolate to UV and NIR has been extensively used in the literature (e.g. Folatelli et al. 2006). The full bolometric light curve of SN 2019cad for $E(B-V)_{\rm Host}=0.0$ mag (red crosses) and $E(B-V)_{\rm Host}=0.49$ mag (dashed line) is presented in the bottom panel of Fig. 2. As seen, the limited photometric coverage at early and late times gives us larger uncertainties during the initial peak as well as a slightly increase in luminosity after 100 d.

To estimate the luminosity of the initial and main peak, together with the slope of the tail, we use GPs. For the bolometric light curve assuming $E(B-V)=0.0$ mag, we find a main peak luminosity of $L_{\rm bol}=5.1\times10^{42}$ erg s^{-1} occurring at 43.6 d. The initial peak happens at 23 d at a luminosity of 1.7×10^{41} erg s^{-1}. After ∼60 d, the bolometric light curve declines at a rate of 5.75 mag per 100 d. These values are much higher than that expected from the ^{56}Co decay, but they are comparable to those obtained for the redder filters in the optical light curves.

3.5 Spectral evolution

Fig. 3 shows the optical spectra of SN 2019cad from 13.6 to 88.1 d past explosion. The first four spectra obtained during the initial peak (before 30 d) display the typical features of an SN Ic (identifications confirmed by the SYNOW (Fisher 2000) fits; see below). At this early phase, the spectra are dominated by strong O I λ7774, Ca II (H&K and NIR triplet) and Fe II lines (around 5000 Å). Si II λ6355 and Na I D are also visible, together with a weak absorption of C II λ6580 and λ7235. From 13.6 to 22.3 d, the bluer part of the spectra diminishes due to Fe II line-blanketing, Si II λ6355 becomes weak, and C II λ6580 completely disappears.

From 40 d past explosion, the spectra of SN 2019cad show a remarkable transformation, which coincides with the main light-curve peak. At 45 d, the spectrum is anew characterized by a blue continuum with weak features of Ca II (H&K and NIR triplet), Na I D, and Fe II. O I λ7774 is now the strongest feature in the spectrum. Si II λ6355, C II λ6580, and λ7235 are visible again after almost complete disappearance at 22.3 d. At 50 d, C II λ6580 and λ7235 become weaker and are undetectable at 53 d. In the same period, the bluer part of the spectra shows three absorption features that correspond to Fe II λλλ4924, 5018, and 5169 lines, together with a clear detection of Sc II λ5531.

Later on, from day 62.8, the Ca II NIR triplet starts to show an emission component, suggesting the start of the nebular phase. Sc II λ5531 becomes stronger, while Sc II λ5663 is clearly detected. On the other hand, Si II λ6355 vanishes. We observe a significant decrease of the flux in the bluer part of the spectra, which is mainly produced by the line-blanketing. In the last observation, at 88.1 d, the spectrum shows a combination of absorption and emission lines. The redder part of the spectrum starts to be dominated by forbidden emission lines of [O I] λλ6300, 6364 and [Ca II] λλ7291, 7323, while the bluer part is still dominated by the iron absorption lines. The Na I D line presents a strong residual absorption component. At this stage, the Ca II NIR triplet is the strongest feature in the spectrum.

To identify the lines in the spectra of SN 2019cad, we use the SYNOW code (Fisher 2000). Fig. 4 shows the best fit obtained for the SN spectra at 13.6 and 45.2 d. For the first spectrum, we assume a blackbody temperature of $T_{\rm bb}=5300$ K and a photospheric velocity

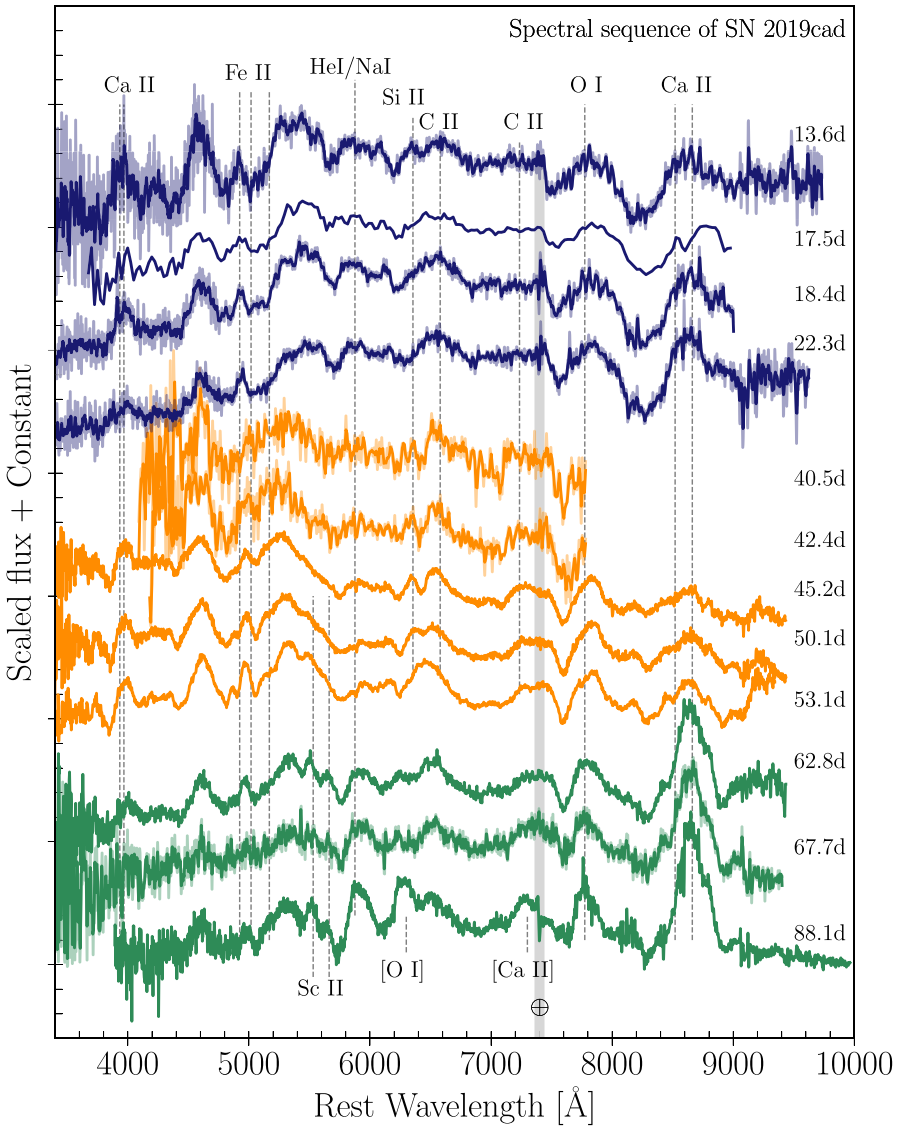

Figure 3. Spectral sequence of SN 2019cad from 13.6 to 88.1 d from explosion. The phases are labelled on the right. Each spectrum has been corrected for Milky Way reddening and shifted vertically by an arbitrary amount for presentation. The vertical dashed lines indicate the rest position of the strongest lines. The colour of the spectra represents the different phases where they were observed: initial peak in blue, main peak in orange, and linear tail in green.

of $v_{ph} = 8600$ km s^{-1}, while for the spectrum at 45.2 d, we use $T_{bb} = 5600$ K and $v_{ph} = 5500$ km s^{-1}. The synthetic spectrum at 13.6 d was obtained including Ca II, O I, Na I D, Si II, Fe II, and C II. Overall, the synthetic spectrum reproduces very well the observed features of SN 2019cad and helps us to confirm the two absorptions near ∼6000 Å as Si II and C II. For the second epoch, the synthetic spectrum contains lines of Ca II, O I, Na I D, Si II, C II, and Ba II. Although we can reproduce most of the lines observed in SN 2019cad, we do not find a great match for the Ca II H & K neither for the continuum in the region between 5500 and 7500 Å. The difficulty to reproduce this second spectrum could be caused by the energy source powering the main peak, which could break some of the assumptions of SYNOW. One interesting characteristic of these two spectra and their respective fits is the strength of the Si II and C II lines. Normally, these lines become weaker over time due to a temperature dependence: their strength decreases as the temperature decreases. However, for SN 2019cad the temperature rises at ∼40 d, and thus the Si II and C II are detected again. The presence of C II in the SN spectra could indicate a significant amount of carbon in the progenitor star.

3.6 Expansion velocities

We measure the expansion velocities of the ejecta from the minimum absorption flux of six spectral features. The velocity evolution of Ca II λλ8498, 8542, 8662 triplet feature, Na I D λ5893 O I λ7774, Fe II λ5169, Si II λ6355, and C II λ6580 is presented in Fig. 5. At earlier phases (before 30 d), all lines have decreasing velocities, as expected for a homologous expansion. After 40 d, the velocities of Ca II and Na I D slightly increase, while for the rest of the lines, they remain nearly constant. The change in the velocity evolution matches with the remarkable transformation observed in the light curves and suggests an additional source of energy. The Ca II NIR triplet has the highest velocity, evolving from ∼13 000 to ∼10 200 km s^{-1}, while the Si II has the lowest one, decreasing from ∼7400 to ∼5200 km s^{-1}.

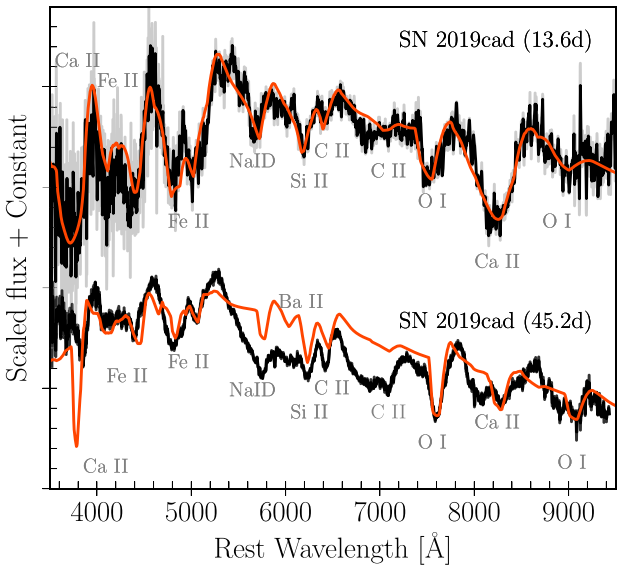

Figure 4. Spectral comparison of SN 2019cad at 13.6 and 45.2 d and the SYNOW fits. The SYNOW synthetic spectra (orange) are overplotted on the observed spectra (black).

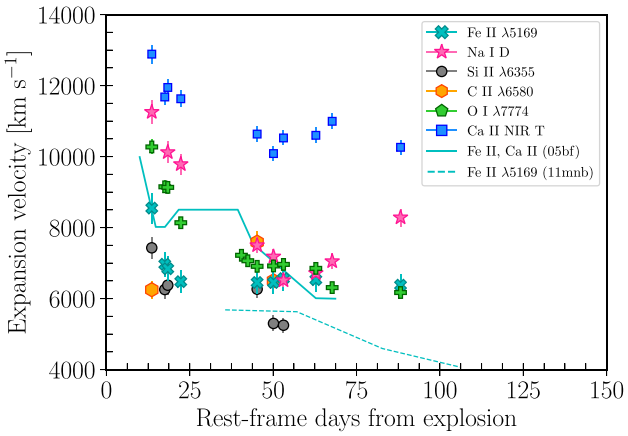

Figure 5. Evolution of expansion velocities of SN 2019cad derived from the minimum of the absorption line. Epochs are with respect to the explosion. For comparison, we also include the Fe II and Ca II velocities of SN 2005bf (Folatelli et al. 2006) and Fe II λ5169 velocities of PTF11mnb (Taddia et al. 2018a).

This behaviour implies that the Ca II lines mainly form in the outer part of the ejecta and Si II lines form in deeper layers. Na I D, Fe II, and O I have intermediate velocities (between ∼11 000 and ∼6000 km s^{-1}). At early phases, Na I D expands faster, followed by O I and Fe II, but after 40 d, all of them have similar velocities (∼7000 km s^{-1}). In general, the velocity range of SN 2019cad is comparable with other normal SN Ic, however, the flat/rising velocity behaviour measured after 40 d is similar to that observed in SN 2005bf (Tominaga et al. 2005; Folatelli et al. 2006) and PTF11mnb (Taddia et al. 2018a).

3.7 Comparison with other SNe

The photometric and spectroscopic evolution of SN 2019cad is unprecedented, however, its double-peaked light curves resemble the Type Ib/c SN 2005bf (Folatelli et al. 2006) and the Type Ic

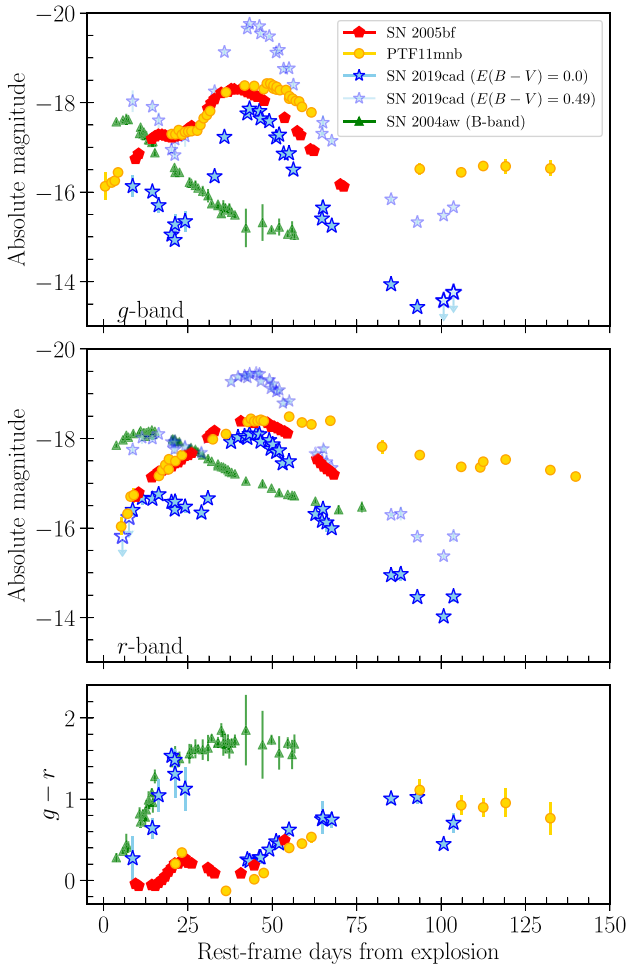

Figure 6. Light curve and colour comparisons. Upper and middle panel: Comparison of the g-band (upper) and r-band (middle) light curves of SN 2019cad (blue stars) with the double-peaked light curves of SN 2005bf (red pentagons) and PTF11mnb (yellow circles), and the normal Type Ic SN 2004aw (green triangles). Please note that for SN 2004aw we use the B and R bands. A light curve of SN 2019cad assuming an $E(B-V)=0.49$ mag is also included for reference. Bottom panel: Colour ($g-r$) curves of SN 2019cad and the comparison sample. Only corrections for Milky Way extinction have been made.

PTF11mnb (Taddia et al. 2018a). From the spectral analysis, we find that SN 2019cad has the characteristic lines of an SN Ic at early times, but around the main peak, the spectra show an unexpected evolution, characterized by a blue continuum and the presence of C II and Si II lines, which had disappeared at ∼20 d (Section 3.5). Looking for objects with similar characteristics, we use SNID (Blondin & Tonry 2007). At early phase (before 30 d), we find a good match with the normal Type Ic SN 2004aw (Taubenberger et al. 2006), however, after the main peak, good spectral matches were not obtained. Based on the common features that SN 2019cad share with SN 2005bf, PTF11mnb (photometrically), and SN 2004aw (spectroscopically), we compare their light curves and spectra in Figs 6 and 7, respectively. Table 2 shows the main parameters measured for the double-peaked light curve SNe and SN 2004aw.

To compare the photometric evolution of these objects in the g and r bands, we present the light curves of SN 2019cad assuming an $E(B-V)=0.0$ mag, but we also correct the light curve for an $E(B-V)=0.49$ mag (clear blue stars). Additionally, we include the normal

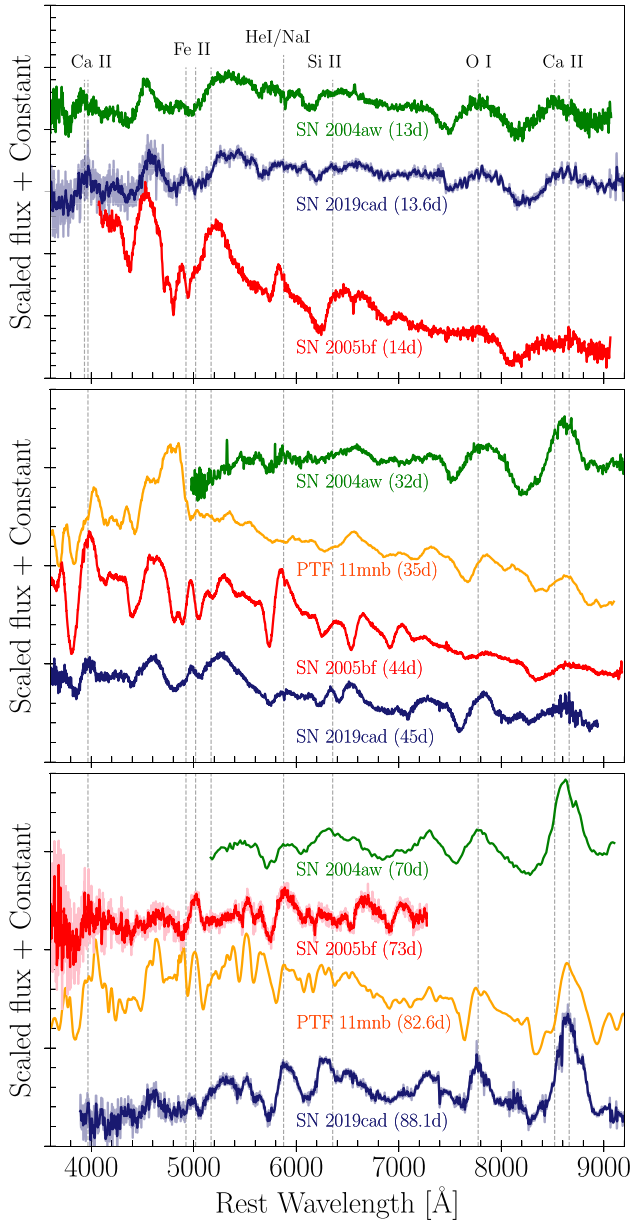

Figure 7. Spectral comparison of SN 2019cad with SN 2005bf, PTF11mnb, and SN 2004aw at three different epochs (13, 40, and 80 d).

Type Ic SN 2004aw (in *B* and *R*). From the light curve comparison (Fig. 6, upper and middle panels), we find that SN 2019cad has a very pronounced initial peak, both in the *g* and *r* bands. While in SN 2005bf and PTF11mnb the initial peak decreases ∼0.5 mag in the *g*, in SN 2019cad the brightness changes more than 1 mag. In the *r* band, only SN 2019cad shows an initial peak. Instead, SN 2005bf and PTF11mnb present a shoulder, which is more conspicuous in PTF11mnb.

Followed by the first maximum, a rise to the main peak is observed in all three objects. Although the brightness in SN 2005bf and PTF11mnb increases ∼1 mag in *g*, in SN 2019cad the rise is around 3 mag in *g* and about 1.8 mag in *r*. For SN 2005bf, the main peak occurs at ∼40 d in *g* and ∼42 d in *r*. PTF11mnb reaches it at ∼46 and ∼52 d, and SN 2019cad at 43.9 and 44.3 d, respectively. SN 2019cad has a main peak that is the most narrow of those shown by these three double-peaked objects. At around 100 d, SN 2005bf has declined by more than 2 mag from peak in *r* band, PTF11mnb only ∼1 mag, and SN 2019cad more than 4 mag.

On the other hand, SN 2004aw shows the typical light curve of an SN Ic, with a main *R*-peak at ∼14 d from the explosion. In terms of luminosity, SN 2004aw is brighter than the initial peak of SN 2019cad (for $E(B-V) = 0.0$ mag), but it is similar in the *r* band when an $E(B-V) = 0.49$ mag is assumed for SN 2019cad. Comparing the luminosity of the double-peaked objects, we find that SN 2019cad is always fainter than SN 2005bf and PTF11mnb in both the initial and main peak for $E(B-V) = 0.0$ mag. However, if an $E(B-V) = 0.49$ mag is assumed, SN 2019cad is >1.5 mag brighter than these two objects.

From the colour curves (Fig. 6, bottom panel), SN 2019cad and SN 2004aw show a similar evolution during the first 20 d, SN 2004aw being slightly redder. In the same period, SN 2005bf and PTF11mnb show colours much bluer than SN 2019cad and SN 2004aw. This behaviour suggests that at early phases SN 2019cad was comparable to any other normal SN Ic, however, after 20 d, the evolution of SN 2019cad changes radically: it becomes rapidly bluer reaching a minimum at ∼44 d (corresponding to the main peak in the light curve). From this epoch, the evolution and colours of SN 2019cad, SN 2005bf, and PTF11mnb are similar.

Fig. 7 presents the spectral comparison of SN 2019cad with SN 2005bf, PTF11mnb, and SN 2004aw at three different epochs: ∼13, ∼40, and ∼80 d from explosion. At around 13 d, SN 2019cad is very similar to the normal Type Ic SN 2004aw. They show strong lines of Ca II, O I, and Fe II. The spectrum of SN 2005bf has a similar Ca II absorption line to SN 2019cad, however, the rest of the spectrum has significant differences, such as weak detection of He I lines, lack of O I, and a strong line around ∼6265 Å, which has been identified as a high-velocity feature of Hα (Folatelli et al. 2006). These properties could indicate that SN 2019cad is similar, but more stripped than SN 2005bf. By ∼40 d, all objects in the comparison sample present very different spectra. Both SN 2019cad and SN 2004aw have a prominent O I line, however, the Ca II absorption feature is shallow in SN 2019cad. For SN 2005bf, the He I lines are exposed, but they are missing in the rest of the objects. SN 2005bf, PTF11mnb, and SN 2019cad have blue spectra compared to SN 2004aw. At this phase, SN 2019cad has prominent lines of C II and Si II, which are not clearly seen in the other objects. At ∼80 d, most of the objects show some signatures of emission lines, which indicate the beginning of the nebular phase. Although SN 2019cad, SN 2005bf, and PTF11mnb have similar light-curve morphology, and comparable colours after 40 d, their spectra are completely different. This spectral diversity could suggest differences in their progenitor stars.

When we compared the evolution of the Fe II velocities of SN 2019cad and those from the double-peaked SN 2005bf and PTF11mnb, we notice that SN 2019cad lies between these two objects (see Fig. 5). Before 15 d, SN 2019cad and SN 2005bf have comparable velocities, but after that the velocity of SN 2019cad continues to decrease, while the velocity of SN 2005bf increases slightly, and then it is flat. PTF11mnb, the object with the lowest velocities, has a flat evolution between 38 and 60 d. A flat evolution is also observed in SN 2019cad later than 40 d.

4 LIGHT-CURVE MODELLING

In order to understand the sources that could be responsible for enhancing the light curve of SN 2019cad, we have explored the main competing ideas that were presented in relation to peculiar

Table 2. Properties of SN 2019cad and the comparison sample.

Parameters	SN 2019cad[1]	SN 2005bf[2]	PTF11mnb[3]	SN 2004aw[4]
Host Galaxy	UGC 4798	MCG + 00-27-5	SDSS J003413.34+024832.9	NGC 3997
Explosion date (MJD)	58550.44 ± 4	53458.00	55804.34 ± 0.5	53080.9
Distance modulus	35.38	34.57	37.14	34.26
Spectroscopic classification	Ic	Ib/c	Ic	Ic
$E(B-V)_{\rm MW}$ (mag)	0.015	0.045	0.016	0.20
$E(B-V)_{\rm Host}$ (mag)	0.0	0.0	0.0	0.35
		***g* band**		
Initial peak magnitude (mag)	−16.35⋆	−17.24	−17.39	–
Initial peak epoch (d)	8	16.2	21.3	–
Main peak magnitude (mag)	−17.83[a]	−18.25	−18.37	−17.63[b]
Main peak epoch (d)	43.9	40	46.3	7
		***r* band**		
Initial peak magnitude (mag)	−16.68[a]	–	–	–
Initial peak epoch (d)	15	–	–	–
Main peak magnitude (mag)	−18.10[a]	−18.44	−18.45	−18.14[b]
Main peak epoch (d)	44.3	42	52.2	14

Notes. References: [1]This work; [2]Folatelli et al. (2006); [3]Taddia et al. (2018a); [4]Taubenberger et al. (2006).
[a]Absolute magnitudes assuming $E(B-V)_{\rm Host}=0$ mag.
[b]For SN 2004aw, we report the *B* (instead *g*) and *R* magnitudes, respectively.

double-peaked SNe, SN 2005bf (Folatelli et al. 2006) and PTF11mnb (Taddia et al. 2018a). Like SN 2019cad, these objects present a rise and decline in luminosity prior to the main peak. Such early behaviour cannot be reconciled with an extended envelope as used to model cooling emission in SNe IIb or by assuming the presence of a small amount of circumstellar material (Bersten et al. 2012; Nakar & Piro 2014). We performed a brief exploration of these possibilities with no success. The main reason was the duration of the SN 2019cad first peak. Assuming the presence of a thin envelope, we can only reproduce a first peak with a duration of less than 10 d and a decreasing luminosity due to the cooling process. As a result of this cooling process and the existence of an additional source that heats the ejecta, usually radioactivity, the light curve shows a minimum. Similar outcome can be obtained assuming the presence of a local and low-mass CSM (see also Jin, Yoon & Blinnikov 2021 for comparable results). Nevertheless, more extreme CSM conditions, as expected to explain hydrogen-rich SNe with narrow emission lines (SN IIn) or some superluminous SNe (SLSNe), could explain the early and/or main peak in the SN light curve. However, we did not explore these possibilities here. Instead, we analysed in detail the following scenarios: (1) a double nickel distribution (Section 4.1) and (2) the first peak powered by nickel but the second one by a magnetar (Section 4.2). In this analysis, we have assumed a zero host extinction (see discussion in Section 3.2).

4.1 Double ^{56}Ni distribution

SN 2019cad is luminous enough to envisage that outflows were involved in its explosion. Several studies (see e.g. MacFadyen, Woosley & Heger 2001; Banerjee & Mukhopadhyay 2013) have considered SNe with outflows or jets in relation to GRB. Jets can induce nucleosynthesis of radioactive elements at the outer layers of the ejecta before the shock front of the SN arrives (Nishimura, Takiwaki & Thielemann 2015). The outer nickel produced in this way could be responsible for the first peak observed in the light curve of SN 2019cad as explored for SN 2005bf (Tominaga et al. 2005; Folatelli et al. 2006), PTF11mnb (Taddia et al. 2018a), and SN 2008D (Bersten et al. 2013). The lack of high-energy emission could be explained by the inability of the jets to breakout the SN surface, or by geometric reasons. Although we did not find any high-emission reported, we cannot rule out their possible existence.

To analyse the double ^{56}Ni possibility, we performed hydrodynamic calculations using different helium-rich progenitors as hydrostatic initial conditions. Specifically, we have tested models with masses of 5 (He5) and 8 $M_\odot$ (He8) at the pre-SNe stage. These models were calculated by Nomoto & Hashimoto (1988) and correspond to main-sequence stars of 18, and 25 $M_\odot$, respectively. A more massive progenitor of 11 $M_\odot$ (He11) corresponding to a main-sequence star of 30 $M_\odot$ computed with MESA code (Paxton et al. 2011) was also used. We have artificially exploded these configurations using the code presented in Bersten, Benvenuto & Hamuy (2011); a one-dimensional radiation hydrodynamical code which assumed flux-limited diffusion approximation and grey transfer for gamma photons produced during the radioactive decay. The code assumes that the positrons are fully trapped all times and fully deposit their energy before annihilation following Sutherland & Wheeler (1984). After several calculations, we found that the highest mass progenitor (He11 in our case) is favoured to explain the double-peaked light curve of SN 2019cad (see Fig. 8). This is because it allows the large temporal departure between the light curve peaks as a consequence of depositing the inner and outer nickel at a larger distance in mass coordinate. For lower mass progenitors, even if the general luminosity trend in the light curve can be reached, the resulting $L_{\rm bol}$ between 20 and 40 d is far above that observed, with the morphology of a minimum around 25 d poorly reproduced.

Our best case was produced by He11 assuming an explosion energy of $E_{\rm exp}=3.5\times10^{51}$ erg, an ejected mass of $M_{\rm ej}=9.5$ $M_\odot$, and the formation of a neutron star of ≈1.5 $M_\odot$. Fig. 8 shows this model compared with the observations of SN 2019cad. The double-peaked morphology of the light curve was obtained assuming the nickel distribution presented in Fig. 9. We have had to consider a concentrated inner component close to the compact remnant (1.5 $M_\odot$), similar to what was found for SN 2005bf (Folatelli et al. 2006), plus an external ^{56}Ni component. In the model presented, the external nickel needs to be close but below the surface to fit the time-scale of the first peak of the light curve. We found that an external ^{56}Ni mass of 0.041 $M_\odot$ satisfied our requirements. This represents a small fraction of the inner component, with a mass of 0.3 $M_\odot$.

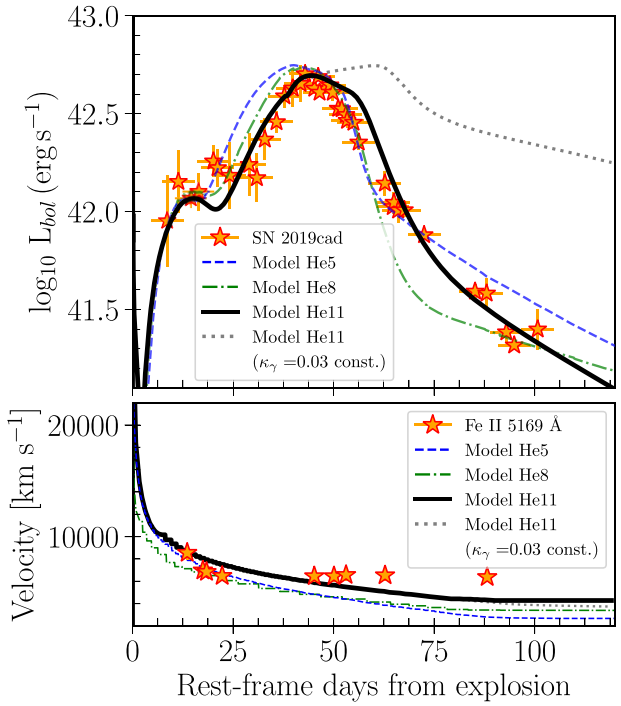

Figure 8. Top panel: Comparison between our preferred double-peaked ^{56}Ni model (black solid line) and the SN observations (orange stars). For this model, we use a progenitor with a pre-SN mass of 11 M$_\odot$ (He11), corresponding to a zero-age main sequence mass of 30 M$_\odot$, an explosion energy of 3.5 × 10^{51} erg, and ejected mass of 9.5 M$_\odot$. For comparison, we also include the double ^{56}Ni distribution models for lower pre-SN masses: 5 (He5; in blue dashed line) and 8 (He8; green dash–dotted line). In all three cases, an enhancement of the gamma-ray leakage is assumed at around the date of *L*-main peak. Models with lower mass produces an earlier main peak and overestimate the rise time luminosity. The He11 model assuming a constant $\kappa_\gamma = 0.03$ (dotted grey line) is also presented as reference. Bottom panel: Evolution of the He11 (black solid line), He5 (in blue dashed line), and He8 (green dash–dotted) line photospheric velocity compared with the Fe II velocity of SN 2019cad.

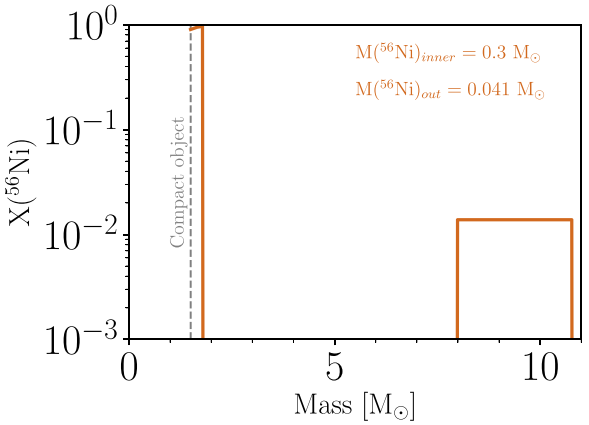

Figure 9. The ^{56}Ni abundance profile of our preferred model powered by the double-peaked nickel distribution. The stellar surface is at 500 R$_\odot$ for ∼11 M$_\odot$ before explosion (i.e. the outer component is not extended up to the surface). Note that the inner component shows a slightly decline due to presence of other heavy elements such as Si, Ar, or Ca.

Table 3. SN 2019cad light-curve modelling parameters.

	$E(B-V)_{\rm Host} = 0.0$ mag	$E(B-V)_{\rm Host} = 0.49$ mag
Double ^{56}Ni distribution model		
Internal ^{56}Ni component	0.300 M$_\odot$	0.904 M$_\odot$
External ^{56}Ni component	0.041 M$_\odot$	0.132 M$_\odot$
Double ^{56}Ni distribution plus magnetar model		
Initial period (P)	11 ms	4 ms
Magnetic field (B)	26 × 10^{14} G	12 × 10^{14} G
External ^{56}Ni component	0.041 M$_\odot$	0.132 M$_\odot$

Other ^{56}Ni distributions have been also explored, in particular, we analysed if a smoother transition between the inner and outer ^{56}Ni component could improve the light-curve modelling, but we did not find substantial differences with the distribution showed in Fig. 9. Therefore, we preferred to set a simplistic case with an inner ^{56}Ni-rich layer (the abundance mimics the one of Si-Ar-Ca, i.e. increasing outward) and an outer component with constant nickel abundance. These are well-departed zones, with no nickel in the middle (see Fig. 9).

In addition to the early peculiar morphology, SN 2019cad shows a steeper decline in the light curve after the main peak, similar to that observed in SN 2005bf. Assuming that this peak was powered by nickel, an artificial reduction in the gamma-ray trapping was proposed to explain the post-peak behaviour of SN 2005bf (Tominaga et al. 2005; Folatelli et al. 2006). An equivalent treatment, as an ad hoc leakage factor used by Vreeswijk et al. (2017), also resembles the incomplete trapping of gamma-rays in Drout et al. (2013). Following this idea, we have modified the gamma-ray opacity from $\kappa_\gamma = 0.03$ to $\kappa_\gamma = 0.0005$ cm^2 g^{-1} around the mean light curve peak of SN 2019cad. By default our code uses a fixed gamma-ray opacity, however this can be changed as required. The values mentioned above implies a decrease of the opacity by a factor of 60, which in turn allows a much larger gamma-ray leakage. We cannot provide a thorough physical justification for this assumption as it was made to fit the rapid light curve post-maximum decline. However, such a reduction of the gamma-ray opacity might be related to the asymmetry of the explosion that produces extremely inhomogeneous ejecta (see also e.g. Maeda et al. 2007).

The model presented reproduces the light-curve properties of SN 2019cad reasonably well: the double-peaked morphology and the fast decline after the peak. However, some discrepancies appear around ≈ 25 d where the observations show a slightly higher luminosity than the model. Finally, we note that, although we have not considered the photospheric velocity evolution in the modelling (which could lead to a possible degeneracy in the parameters found, see discussion in Martinez et al. 2020 and references therein), the model gives a relatively good representation of the Fe II λ5169 velocities as shown in the bottom panel of Fig. 8.

While we consider an $E(B-V)_{\rm Host} = 0.0$ mag for our analysis, we also explore the effects of having an $E(B-V)_{\rm Host} = 0.49$ mag. As shown in the bottom panel of Fig. 2, the main effect of assuming non-negligible extinction is to increase the luminosity, and at first order, we can consider that the shape of the light curve remains similar. An increase in luminosity can be produced assuming a larger nickel mass. To reproduce a brighter light curve, our model requires an external nickel component of 0.132 M$_\odot$ and an internal component of 0.904 M$_\odot$. These values are ∼3 times higher than our original model. Table 3 summarizes the values that better reproduce the light curve of SN 2019cad assuming an $E(B-V)_{\rm Host} = 0.0$ and 0.49 mag, respectively.

4.2 Magnetar

The idea that a strongly magnetized neutron star or magnetar could have been the powering source of the main peak in SN 2005bf was proposed by Maeda et al. (2007). Late-time photometry of SN 2005bf has provided further support to this idea.

The research on young magnetars into SNe has vastly grown in last years, with suggestions for regular (see e.g. Sukhbold & Thompson 2017), bright (Inserra et al. 2013; Dessart & Audit 2018; Orellana, Bersten & Moriya 2018), and peculiar SNe (Bersten et al. 2016; Woosley 2018). Recent results provide new insights about the magnetar properties. Detailed simulations have shown that magnetars can accelerate iron-group elements deep in the ejecta, and explain the high-velocity Fe lines observed in some core-collapse SNe (Chen, Woosley & Whalen 2020). Another interesting characteristic is that the magnetar creation might be accompanied by jets (e.g. Soker 2016). Based on this assumption, we propose that a magnetar and a double nickel distribution can, in principle, be combined. To explore this possibility for SN 2019cad, we applied a version of the hydrodynamical code that incorporates the extra power source of magnetar (Bersten et al. 2016) and assumes that this energy is deposited at the inner layers of the ejecta. For the low-mass progenitors we did not find a promising case, therefore the He11 configuration was again preferred. We performed a wide exploration of the magnetar parameter space, for fixed standard properties of the neutron star, and assuming the spin-down proceeds through vacuum dipole radiation (braking index $n = 3$). We obtained an acceptable match for the main peak for $P \sim 11$ ms and $B \sim 26 \times 10^{14}$ G (see Fig. 10), with an explosion energy of $E_{\rm exp} = 3.5 \times 10^{51}$ erg and a conservative ^{56}Ni mass ($\sim$0.05 M$_\odot$) at the inner layers of the progenitor. This inner nickel mass is constrained by the observations at the tail of the light curve. We set the gamma-opacity to a usual value, $\kappa_\gamma = 0.03$ cm^2 g^{-1} during the complete evolution. Note that the energy of the magnetar is assumed to be deposited at the inner layers of the ejecta as internal energy. The magnetar model alone cannot reproduce the two peaks observed in the light curve of SN 2019cad. Therefore, we resume to the presence of some external nickel, and turn on the same configuration of the outer $\sim$0.04 M$_\odot$ ^{56}Ni depicted in Fig. 9.

In the hybrid model proposed for PTF11mnb (Taddia et al. 2018a), the magnetar-powered light curve is explored through the semianalytic prescription of Kasen & Bildsten (2010) in combination with the diffusion one-zone model of Arnett (1982) for the ^{56}Ni radioactive decay. In order to obtain the maximum time-scale with that treatment, the magnetar must ignite with a delay of several days from the explosion. We note the physical difficulty to explain such delay. The simulations of post-collapse are consistent with evolutionary time-scales of seconds between the proto-neutron star birth and the moment when the stable neutron star holds the high angular momentum and strong magnetic field to initiates the spin-down phase (Mezzacappa et al. 2001; Metzger, Thompson & Quataert 2007; Aloy & Obergaulinger 2021). However, in our hydrodynamical implementation of the magnetar model assuming a massive (He11) progenitor, such delay was not needed and the magnetar was turned-on at the same time as the SN explosion, providing a more reliable prescription. In addition, this model did not require a reduction of the gamma-ray opacity.

Lastly, we explore the parameter space required to model a brighter light curve (assuming an $E(B-V)_{\rm Host} = 0.49$ mag, see Fig. 2). As shown in Fig. 10, in our double ^{56}Ni distribution plus magnetar model, the effect of the magnetar is more important for the main peak, while the impact of the ^{56}Ni mass is significant for the initial peak.

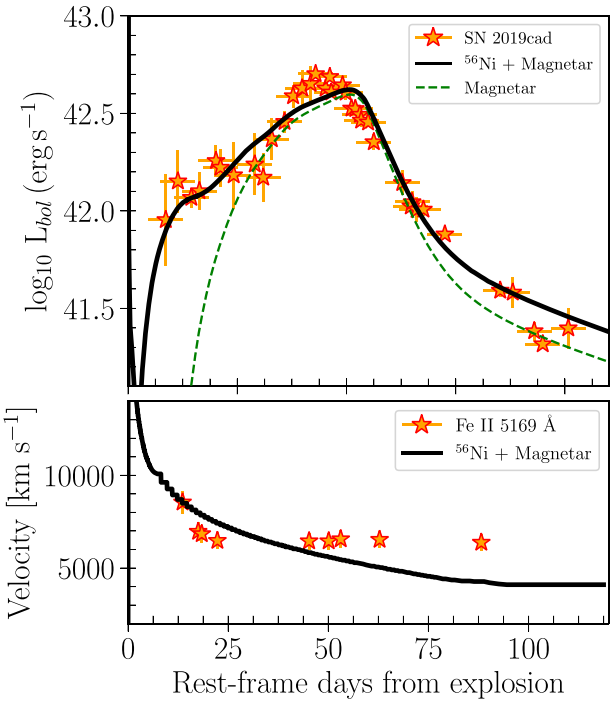

Figure 10. Top panel: The magnetar plus nickel model for a progenitor mass of 11 M$_\odot$ (see Section 4.2) compared with the light curve of SN 2019cad. For the first maximum, an outer ^{56}Ni mass of 0.041 M$_\odot$ is assumed. The second, main peak was modelled with an inner mass of ^{56}Ni 0.05 M$_\odot$ and a magnetar with an initial period $P = 11$ ms and a magnetic field of $B = 26 \times 10^{14}$ G (dashed line). The calculated light curve with both ^{56}Ni components and the magnetar is shown in black solid line. Bottom panel: Evolution of the magnetar plus nickel model photospheric velocity compared with the Fe II velocity of SN 2019cad.

It has been shown that in a magnetar, the peak luminosity is mostly affected by the initial period (P) and the magnetic field (B) (e.g. Kasen & Bildsten 2010; Dessart 2019). Taking these three parameters (P, B, and ^{56}Ni mass) into account, we can reproduce the new light curve. To reach the main-peak luminosity, while preserving its time-scale, a magnetar with $P \sim 4$ ms and $B \sim 12 \times 10^{14}$ G is necessary. To reproduce the initial peak, we need to include an external nickel component of 0.132 M$_\odot$. These parameters, summarized in Table 3, are within the range of previously published values (e.g. Dessart 2019 for the magnetar and Anderson 2019, for the ^{56}Ni mass).

5 DISCUSSION AND CONCLUSIONS

We have presented the spectroscopic and photometric analysis of the Type Ic SN 2019cad during the first 100 d from explosion. Located at a projected distance of 4.6 kpc from the centre of H II-rich galaxy UGC 4798, SN 2019cad presents an uncommon light-curve evolution, which resembles the peculiar Type Ib/c SN 2005bf and the Type Ic PTF11mnb. That is, an initial peak at about 10–15 d from explosion followed by a main peak at $\sim$45 d from explosion. While the luminosity of the first peak (M$_r = -16.68$ mag) is within the ranges of normal hydrogen-free events (e.g. Taddia et al. 2018a), the second one (M$_r^{max} = -18.10$ mag) is brighter than normal, but consistent with that observed in double-peaked SNe, if the extinction is $E(B-V) = 0$ mag. From the spectroscopic point of view, SN 2019cad shows important differences with respect to SN 2005bf and PTF11mnb. During the first 30 d (first peak), the spectra of

SN 2019cad are comparable with typical SNe Ic, however, when the light curve goes up to the main peak (at around 45 d), the spectra display an unusual transformation, easily noticeable by the presence of the Si II and C II lines. The presence of these lines were confirmed by the SYNOW fits. At these later epochs, no spectral matches were found, suggesting that SN 2019cad has a unique evolution.

To try to understand the peculiar photometric behaviour of SN 2019cad, we have explored two possible scenarios, both assuming a progenitor with a pre-SN mass of 11 $M_\odot$, corresponding to a zero-age main sequence mass of 30 $M_\odot$, an explosion energy of 3.5×10^{51} erg, and ejected mass of 9.5 $M_\odot$, assuming the formation of a compact object with a 1.5 $M_\odot$ and a double-peaked ^{56}Ni distribution, with an outer, though below the surface, low-mass component of 0.04 $M_\odot$. For the main peak we obtained (1) an inner nickel component of 0.3 $M_\odot$ (Section 4.1); or (2) a ^{56}Ni plus magnetar model (Section 4.2). Specifically, the magnetar properties found are an initial rotation period $P \sim 11$ms and magnetic field strength of $B \sim 26 \times 10^{14}$ G. A discussion of how the neutron star properties can affect the values of P and B can be found in Bersten et al. (2016). With this in mind, as well as other simplifications of the 1D model, the parameters obtained here for the magnetar should be considered approximate values.

While either model can reproduce the overall morphology observed in SN 2019cad, the double ^{56}Ni distribution model provided a bit better representation of the double-peaked light curve. However, to reproduce the late ($t > 60$ d) behaviour of fast decline post-maximum, we artificially reduced the gamma-ray trapping. Similar approaches were explored by Tominaga et al. (2005) and Folatelli et al. (2006) to fit the decline observed in SN 2005bf, but this was not necessary in the case of SN PTF11mnb. For the magnetar model, an internal component of ^{56}Ni can be present, involving at most some 0.05 $M_\odot$. The gamma opacity was not needed to be reduced. The drawback in this case is the worse fit of the bolometric light curve at the transition (around $t = 25$ d) and up to the main peak.

The amount of nickel found for the double ^{56}Ni distribution model is larger than the expected for hydrogen-free SNe (see e.g. Prentice et al. 2016; Taddia et al. 2018b; Anderson 2019), while for the model including the magnetar is within the range of these objects. The progenitor mass (pre-SN mass of 11 $M_\odot$, corresponding to a zero-age main sequence mass of 30 $M_\odot$) is also large, but comparable with that of SN 2005bf (Tominaga et al. 2005; Folatelli et al. 2006; Maeda et al. 2007). The outer ^{56}Ni component in the stellar interior that we assumed to be related with jets could be hinted by high-energy emission as in GRB-SNe explosions. Although, as this SN is quite peculiar, it may be a failed GRB (Huang, Dai & Lu 2002) i.e. having jet-like outflows without sufficient Lorentz factor, or even a GRB with collimated jets that do not point in the direction of the observer. Archival searches for detections of SN2019cad at other wavelengths are therefore encouraged.

As discussed in Section 3.2, considerable discrepancies in the reddening estimation for SN 2019cad were found with different methods, and an $E(B-V)_{\rm Host} = 0.0$ mag was adopted for our analysis. However, based on the strong narrow Na I D absorption feature detected in the spectra, we deduce that SN 2019cad may suffer a significant reddening. In Section 3.7, we compared SN 2019cad with similar objects and briefly discussed the implications of a higher reddening. By adopting an $E(B-V)_{\rm Host} = 0.49$ mag, we found that the light curve has a significant increase in brightness. To reach the new luminosity by using the double ^{56}Ni distribution model, an external nickel component of 0.132 $M_\odot$ and a value of 0.904 $M_\odot$ for the internal component were needed. We note that a ^{56}Ni mass of 0.904 $M_\odot$ is huge compared with the values measured in normal stripped-envelope SNe (mean value of 0.293 $M_\odot$; Anderson 2019), and is beyond those estimated for even extreme objects such as GRB-SNe (∼0.3–0.6 $M_\odot$; e.g. Cano et al. 2017). These gigantic values disfavour this model. On the other hand, assuming a magnetar model, the luminosity could be easily reach by changing the initial period and the magnetic field. However, as our model requires nickel to reproduce the initial peak, an increase in the nickel mass is essential. In our preferred case, the external nickel component is, again, 0.132 $M_\odot$, but $P \sim 4$ ms, which is a few times larger than the theoretical limit for break-up ($P \sim 2$ ms; Dessart 2019). In order to maintain the time of the maximum in the light curve, the magnetic field should be $B \sim 12 \times 10^{14}$ G. These values favour the double ^{56}Ni plus magnetar scenario.

Summarizing, SN 2019cad is within a rare type of event, with only two previous examples, SN 2005bf and PTF11mnb. Despite showing some similar features, these three SNe do show key differences. The similarities in the light curve could suggest a similar explosion mechanism, while the diversity in the spectra could imply different progenitor evolution, e.g. distinctive grades of mass-loss. Although we have found two models that can explain the main photometric properties of SN 2019cad, there are still many issues in our understanding of these objects and the ultimate source of energy to power them is still a mystery.

ACKNOWLEDGEMENTS

We thank the anonymous referee for the comments and suggestions that have helped to improve the paper.

We are grateful to Peter Jonker who enabled the WHT observation of this target during his program W19AN003. We thank Peter Brown its contribution with data from the Neil Gehrels *Swift* Observatory.

CPG and MS acknowledge support from EU/FP7-ERC grant No. (615929). MO acknowledges support from UNRN PI2018 40B696 grant. GP acknowledges support by ANID - Millennium Science Initiative - ICN12_009. NER acknowledges support from MIUR, PRIN 2017 (grant 20179ZF5KS). MF is supported by a Royal Society - Science Foundation Ireland University Research Fellowship. SM acknowledges support from the Magnus Ehrnrooth foundation. AR acknowledges support from ANID BECAS/DOCTORADO NACIONAL 21202412. TMR acknowledges the financial support of the Jenny and Antti Wihuri foundation and the Vilho, Yrjö and Kalle Väisälä Foundation of the Finnish academy of Science and Letters. MS is supported by generous grants from VILLUM FONDEN (13261, 28021) and by a project grant (8021-00170B) from the Independent Research Fund Denmark. LG was funded by the European Union's Horizon 2020 research and innovation programme under the Marie Skłodowska-Curie grant agreement No. 839090. JB, DH, DAH, and CP were supported by NSF grant AST-1911225. TMB was funded by the CONICYT PFCHA/DOCTORADOBECAS CHILE/2017-72180113.

This work has been partially supported by the Spanish grant PGC2018-095317-B-C21 within the European Funds for Regional Development (FEDER).

Based on observations made with the Nordic Optical Telescope, owned in collaboration by the University of Turku and Aarhus University, and operated jointly by Aarhus University, the University of Turku and the University of Oslo, representing Denmark, Finland and Norway, the University of Iceland and Stockholm University at the Observatorio del Roque de los Muchachos, La Palma, Spain, of the Instituto de Astrofisica de Canarias.

Observations from the NOT were obtained through the NUTS and NUTS2 collaboration which are supported in part by the Instrument

Centre for Danish Astrophysics (IDA). The data presented here were obtained in part with ALFOSC, which is provided by the Instituto de Astrofisica de Andalucia (IAA) under a joint agreement with the University of Copenhagen and NOTSA.

Based on observations made with the GTC telescope, in the Spanish Observatorio del Roque de los Muchachos of the Instituto de Astrofísica de Canarias, under Director's Discretionary Time.

This work has made use of data from the Asteroid Terrestrial-impact Last Alert System (ATLAS) project. ATLAS is primarily funded to search for near-earth asteroids through NASA grants NN12AR55G, 80NSSC18K0284, and 80NSSC18K1575; by products of the NEO search include images and catalogues from the survey area. The ATLAS science products have been made possible through the contributions of the University of Hawaii Institute for Astronomy, the Queen's University Belfast, the Space Telescope Science Institute, and the South African Astronomical Observatory.

The Liverpool Telescope is operated on the island of La Palma by Liverpool John Moores University in the Spanish Observatorio del Roque de los Muchachos of the Instituto de Astrofisica de Canarias with financial support from the UK Science and Technology Facilities Council. This work makes use of data from the Las Cumbres Observatory network.

Facilities: ATLAS; GTC; Las Cumbres Observatory; LT; NOT; Swift, WHT, ZTF.

Software: PYTHON from https://www.python.org/, PHOTUTILS (Bradley et al. 2019), ASTROPY (Astropy Collaboration 2018), IRAF, SNOoPY (Cappellaro 2014), FDSTFAST, FLOYDS_PIPELINE (Valenti et al. 2014), GEORGE (Ambikasaran et al. 2015), SYNOW (Fisher 2000), MESA (Paxton et al. 2011), SNID (Blondin & Tonry 2007).

DATA AVAILABILITY

The data underlying this article are available in the Appendix A (Tables A1–A5) and through the WISeREP (https://wiserep.weizmann.ac.il/home) archive (Yaron & Gal-Yam 2012).

REFERENCES

Ahumada R. et al., 2020, ApJS, 249, 3
Aloy M. Á., Obergaulinger M., 2021, MNRAS, 500, 4365
Ambikasaran S., Foreman-Mackey D., Greengard L., Hogg D. W, O'Neil M., 2015, IEEE Trans. Pattern Anal. Mach. Intell., 38, 252
Anderson J. P., 2019, A&A, 628, A7
Anderson J. P., Soto M., 2013, A&A, 550, A69
Anupama G. C., Sahu D. K., Deng J., Nomoto K., Tominaga N., Tanaka M., Mazzali P. A., Prabhu T. P., 2005, ApJ, 631, L125
Arnett W. D., 1982, ApJ, 253, 785
Astropy Collaboration, 2018, AJ, 156, 123
Banerjee I., Mukhopadhyay B., 2013, ApJ, 778, 8
Bellm E. C. et al., 2019, PASP, 131, 018002
Bersten M. C. et al., 2012, ApJ, 757, 31
Bersten M. C., Benvenuto O., Hamuy M., 2011, ApJ, 729, 61
Bersten M. C., Tanaka M., Tominaga N., Benvenuto O. G., Nomoto K., 2013, ApJ, 767, 143
Bersten M. C., Benvenuto O. G., Orellana M., Nomoto K., 2016, ApJ, 817, L8
Bian F. Y., Lou Y. Q., Wang X. F., Yang Y., Qiu Y. L., 2005, Cent. Bur. Electron. Telegrams, 335, 1
Bianco F. B. et al., 2014, ApJS, 213, 19
Blagorodnova N. et al., 2018, PASP, 130, 035003
Blondin S., Tonry J. L., 2007, ApJ, 666, 1024
Bradley L. et al., 2019, astropy/photutils: v0.6
Brown P. J. et al., 2009, AJ, 137, 4517
Brown T. M. et al., 2013, PASP, 125, 1031
Burke J., Hiramatsu D., Arcavi I., Howell D. A., Mccully C., Valenti S., 2019, Transient Name Serv. Classif. Rep., 427, 1
Campana S. et al., 2006, Nature, 442, 1008
Cano Z., Wang S.-Q., Dai Z.-G., Wu X.-F., 2017, Adv. Astron., 2017, 8929054
Cao Y. et al., 2013, ApJ, 775, L7
Cappellaro E., 2014, SNOoPY: a package for SN photometry. Available at: http://sngroup.oapd.inaf.it/snoopy.html
Cenko S. B. et al., 2006, PASP, 118, 1396
Chambers K. C. et al., 2016, preprint (arXiv:1612.05560)
Chen Y.-M. et al., 2012, MNRAS, 421, 314
Chen K.-J., Woosley S. E., Whalen D. J., 2020, ApJ, 893, 99
Cormier D. et al., 2016, MNRAS, 463, 1724
Crowley T. et al., 2013, Cent. Bur. Electron. Telegrams, 3411, 1
de Vaucouleurs G., de Vaucouleurs A., Corwin Herold G. J., Buta R. J., Paturel G., Fouque P., 1991, Third Reference Catalogue of Bright Galaxies. Volume I: Explanations and references. Volume II: Data for galaxies between 0h and 12h. Volume III: Data for galaxies between 12h and 24h. Springer, New York, NY, p. 621
Dessart L., 2019, A&A, 621, A141
Dessart L., Audit E., 2018, A&A, 613, A5
Dessart L., Hillier D. J., Li C., Woosley S., 2012, MNRAS, 424, 2139
Drake A. J. et al., 2009, ApJ, 696, 870
Drout M. R. et al., 2011, ApJ, 741, 97
Drout M. R. et al., 2013, ApJ, 774, 58
Eldridge J. J., Izzard R. G., Tout C. A., 2008, MNRAS, 384, 1109
Elias-Rosa N. et al., 2014, Astron. Telegram, 6628, 1
Filippenko A. V., 1997, ARA&A, 35, 309
Firth R. E. et al., 2015, MNRAS, 446, 3895
Fisher A. K., 2000, PhD thesis, Univ. Oklahoma
Folatelli G. et al., 2006, ApJ, 641, 1039
Folatelli G. et al., 2016, ApJ, 825, L22
Gal-Yam A., 2017, in Alsabti A. W., Murdin P., eds, Observational and Physical Classification of Supernovae, Handbook of Supernovae. Springer International Publishing, Cham, New York, p. 195
Georgy C., Meynet G., Walder R., Folini D., Maeder A., 2009, A&A, 502, 611
Graham M. J. et al., 2019, PASP, 131, 078001
Gutiérrez C. P. et al., 2020, MNRAS, 496, 95
Heger A., Fryer C. L., Woosley S. E., Langer N., Hartmann D. H., 2003, ApJ, 591, 288
Huang Y. F., Dai Z. G., Lu T., 2002, MNRAS, 332, 735
Inserra C. et al., 2013, ApJ, 770, 128
Izzo L. et al., 2019, Nature, 565, 324
Jin H., Yoon S.-C., Blinnikov S., 2021, AJ, 910, 68
Kasen D., Bildsten L., 2010, ApJ, 717, 245
Kilpatrick C. D. et al., 2018, MNRAS, 480, 2072
Kilpatrick C. D. et al., 2021, MNRAS. Available at: https://doi.org/10.1093/mnras/stab838
Lyman J. D., Bersier D., James P. A., Mazzali P. A., Eldridge J. J., Fraser M., Pian E., 2016, MNRAS, 457, 328
MacFadyen A. I., Woosley S. E., Heger A., 2001, ApJ, 550, 410
Maeda K. et al., 2007, ApJ, 666, 1069
Magnier E. A. et al., 2020, ApJS, 251, 6
Makarov D., Prugniel P., Terekhova N., Courtois H., Vauglin I., 2014, A&A, 570, A13
Martinez L., Bersten M. C., Anderson J. P., González-Gaitán S., Förster F., Folatelli G., 2020, A&A, 642, A143
Matheson T., Filippenko A. V., Li W., Leonard D. C., Shields J. C., 2001, AJ, 121, 1648
Mattila S., Smartt S. J., Eldridge J. J., Maund J. R., Crockett R. M., Danziger I. J., 2008, ApJ, 688, L91
Mazzali P. A. et al., 2008, Science, 321, 1185
Metzger B. D., Thompson T. A., Quataert E., 2007, ApJ, 659, 561
Meza N., Anderson J. P., 2020, A&A, 641, A177
Mezzacappa A., Liebendörfer M., Messer O. E., Hix W. R., Thielemann F.-K., Bruenn S. W., 2001, Phys. Rev. Lett., 86, 1935
Modjaz M. et al., 2014, AJ, 147, 99

Modjaz M., Kirshner R., Challis P., Blondin S., Berlind P., 2005, IAU Circ., 8650, 2
Modjaz M., Kewley L., Bloom J. S., Filippenko A. V., Perley D., Silverman J. M., 2011, ApJ, 731, L4
Modjaz M., Gutiérrez C. P., Arcavi I., 2019, Nat. Astron., 3, 717
Munari U., Zwitter T., 1997, A&A, 318, 269
Nakar E., Piro A. L., 2014, ApJ, 788, 193
Nishimura N., Takiwaki T., Thielemann F.-K., 2015, ApJ, 810, 109
Nomoto K., Hashimoto M., 1988, Phys. Rep., 163, 13
Nomoto K. I., Iwamoto K., Suzuki T., 1995, Phys. Rep., 256, 173
Nordin J., Brinnel V., Giomi M., Santen J. V., Gal-yam A., Yaron O., Schulze S., 2019, Transient Name Serv. Discovery Rep., 415, 1
Orellana M., Bersten M. C., Moriya T. J., 2018, A&A, 619, A145
Paxton B., Bildsten L., Dotter A., Herwig F., Lesaffre P., Timmes F., 2011, ApJS, 192, 3
Pettini M., Pagel B. E. J., 2004, MNRAS, 348, L59
Piascik A. S. et al., 2014, in Ramsay S. K., McLean I. S., Takami H., eds, Proc. SPIE Conf. Ser. Vol. 9147, Ground-based and Airborne Instrumentation for Astronomy V. SPIE, Bellingham, p. 91478H
Pignata G. et al., 2011, ApJ, 728, 14
Podsiadlowski P., Joss P. C., Hsu J. J. L., 1992, ApJ, 391, 246
Poznanski D., Ganeshalingam M., Silverman J. M., Filippenko A. V., 2011, MNRAS, 415, L81
Poznanski D., Prochaska J. X., Bloom J. S., 2012, MNRAS, 426, 1465
Prentice S. J. et al., 2016, MNRAS, 458, 2973
Rigault M. et al., 2019, A&A, 627, A115
Schlafly E. F., Finkbeiner D. P., 2011, ApJ, 737, 103
Shivvers I. et al., 2019, MNRAS, 482, 1545
Skrutskie M. F. et al., 2006, AJ, 131, 1163
Smartt S. J., Eldridge J. J., Crockett R. M., Maund J. R., 2009, MNRAS, 395, 1409
Smith K. W. et al., 2019, Res. Notes Am. Astron. Soc., 3, 26
Smith K. W. et al., 2020, PASP, 132, 085002
Smith N., Gehrz R. D., Campbell R., Kassis M., Le Mignant D., Kuluhiwa K., Filippenko A. V., 2011, MNRAS, 418, 1959
Soderberg A. M. et al., 2008, Nature, 453, 469
Soker N., 2016, New Astron., 47, 88
Steele I. A. et al., 2004, in Oschmann Jacobus M. J., ed., Proc. SPIE Conf. Ser. Vol. 5489, Ground-based Telescopes. SPIE, Bellingham, p. 679
Stritzinger M. D. et al., 2018, A&A, 609, A135
Sukhbold T., Thompson T. A., 2017, MNRAS, 472, 224
Sutherland P. G., Wheeler J. C., 1984, ApJ, 280, 282
Taddia F. et al., 2015, A&A, 574, A60
Taddia F. et al., 2018a, A&A, 609, A106
Taddia F. et al., 2018b, A&A, 609, A136
Taubenberger S. et al., 2006, MNRAS, 371, 1459
Thöne C. C., Michałowski M. J., Leloudas G., Cox N. L. J., Fynbo J. P. U., Sollerman J., Hjorth J., Vreeswijk P. M., 2009, ApJ, 698, 1307
Tomasella L., Benetti S., Cappellaro E., Pastorello A., Turatto M., Ochner P., Elias-Rosa N., Morales-Garoffolo A., 2013, Astron. Telegram, 4796, 1
Tominaga N. et al., 2005, ApJ, 633, L97
Tonry J. L. et al., 2018, PASP, 130, 064505
Turatto M., Benetti S., Cappellaro E., 2003, in Hillebrandt W., Leibundgut B., eds, From Twilight to Highlight: The Physics of Supernovae, ESO/MPA/MPE Workshop Garching. Springer, Berlin, Heidelberg, p. 200
Valenti S. et al., 2014, MNRAS, 438, L101
Van Dyk S. D. et al., 2018, ApJ, 860, 90
Van Dyk S. D., 2017, Phil. Trans. R. Soc., 375, 20160277
Van Dyk S. D., Garnavich P. M., Filippenko A. V., Höflich P., Kirshner R. P., Kurucz R. L., Challis P., 2002, PASP, 114, 1322
Van Dyk S. D., Li W., Filippenko A. V., 2003, PASP, 115, 1289
Vreeswijk P. M. et al., 2017, ApJ, 835, 58
Wang J. et al., 2013, MNRAS, 433, 270
Williamson M., Kerzendorf W., Modjaz M., 2021, ApJ, 908, 150
Woosley S. E., 2018, ApJ, 863, 105
Woosley S. E., Bloom J. S., 2006, ARA&A, 44, 507
Woosley S. E., Hartmann D., Pinto P. A., 1989, ApJ, 346, 395
Woosley S. E., Eastman R. G., Weaver T. A., Pinto P. A., 1994, ApJ, 429, 300
Xiang D. et al., 2019, ApJ, 871, 176
Yaron O., Gal-Yam A., 2012, PASP, 124, 668

APPENDIX: TABLES

Photometry and spectroscopic observations of SN 2019cad.

Table A1. ATLAS AB optical photometry.

UT date	MJD	Phase (d)*	Band	Magnitude (mag)
20190227	58542.48	–	*o*	>20.50
20190303	58546.46	–	*o*	>20.50
20190307	58550.44	–	*o*	>20.70
20190311	58554.42	3.88	*o*	19.91 ± 0.11
20190315	58558.43	7.78	*o*	19.45 ± 0.20
20190319	58562.39	11.64	*o*	18.43 ± 0.13
20190323	58566.41	15.55	*o*	18.44 ± 0.11
20190325	58568.41	17.50	*o*	18.63 ± 0.06
20190329	58572.39	21.38	*o*	18.54 ± 0.04
20190402	58576.43	25.31	*c*	19.45 ± 0.05
20190404	58578.40	27.23	*o*	18.74 ± 0.08
20190406	58580.40	29.18	*c*	19.43 ± 0.10
20190408	58582.37	31.10	*o*	18.63 ± 0.07
20190414	58588.39	36.96	*o*	17.64 ± 0.09
20190416	58590.36	38.88	*o*	17.35 ± 0.02
20190420	58594.34	42.76	*o*	17.33 ± 0.03
20190422	58596.34	44.71	*o*	17.41 ± 0.01
20190424	58598.32	46.63	*o*	17.46 ± 0.02
20190426	58600.33	48.59	*o*	17.47 ± 0.02
20190430	58604.34	52.50	*c*	18.04 ± 0.03
20190506	58610.30	58.30	*o*	18.65 ± 0.06
20190508	58612.27	60.22	*c*	18.76 ± 0.05
20190510	58614.27	62.17	*o*	18.77 ± 0.08
20190512	58616.27	64.12	*o*	18.71 ± 0.08
20190514	58618.29	66.09	*o*	19.16 ± 0.26
20190516	58620.31	68.05	*o*	19.34 ± 0.15
20190518	58622.26	69.95	*o*	19.47 ± 0.30
20190522	58626.24	73.83	*o*	19.40 ± 0.13
20190524	58628.25	75.79	*o*	19.32 ± 0.28
20190530	58634.25	81.63	*o*	19.57 ± 0.23
20190601	58636.25	83.58	*c*	22.28 ± 0.42

Note. *Rest-frame phase in days from explosion, MJD = 58550.44 ± 4.

Table A2. Optical photometry of SN 2019cad.

UT date	MJD	Phase (d)*	*u* (mag)	*B* (mag)	*V* (mag)	*g* (mag)	*r* (mag)	*i* (mag)	*z* (mag)	Telescope‡
20190322	58565.32	14.49	$20.10 \pm 0.10^{\star}$	20.05 ± 0.09	19.25 ± 0.06	19.43 ± 0.04	18.77 ± 0.03	18.73 ± 0.03	–	LCOGT
20190328	58571.11	20.13	–	21.24 ± 0.07	19.27 ± 0.03	20.39 ± 0.03	18.84 ± 0.03	18.58 ± 0.04	–	LCOGT
20190329	58572.17	21.16	–	21.49 ± 0.07	19.58 ± 0.03	20.51 ± 0.05	19.01 ± 0.03	18.77 ± 0.03	–	LCOGT
20190421	58594.85	43.26	18.44 ± 0.02	–	–	17.58 ± 0.03	17.32 ± 0.02	17.19 ± 0.02	17.05 ± 0.02	LT
20190423	58596.86	45.21	–	–	–	–	17.31 ± 0.02	–	–	NOT
20190424	58597.85	46.18	18.66 ± 0.02	–	–	17.63 ± 0.02	17.33 ± 0.01	17.14 ± 0.01	17.07 ± 0.02	LT
20190427	58600.85	49.10	18.69 ± 0.02	–	–	17.86 ± 0.03	17.46 ± 0.01	17.26 ± 0.01	17.16 ± 0.02	LT
20190428	58601.90	50.12	–	–	–	–	17.55 ± 0.03	–	–	NOT
20190429	58602.95	51.14	–	–	–	18.22 ± 0.01	17.72 ± 0.01	17.56 ± 0.01	17.37 ± 0.01	NOT
20190430	58603.85	52.02	19.61 ± 0.02	–	–	18.16 ± 0.02	17.69 ± 0.02	17.48 ± 0.02	17.30 ± 0.02	LT
20190501	58604.92	53.06	–	–	–	–	17.98 ± 0.08	–	–	NOT
20190503	58606.85	54.94	–	–	–	18.57 ± 0.06	17.93 ± 0.03	17.73 ± 0.03	17.55 ± 0.03	LT
20190511	58614.88	62.76	–	–	–	–	19.11 ± 0.10	–	–	NOT
20190513	58616.89	64.72	21.99 ± 0.24	–	–	20.03 ± 0.03	19.26 ± 0.03	18.84 ± 0.03	18.47 ± 0.02	NOT
20190516	58619.85	67.60	>21.71	–	–	20.19 ± 0.09	19.43 ± 0.04	19.05 ± 0.03	18.55 ± 0.03	NOT
20190603	58637.90	85.19	–	22.23 ± 0.10	–	21.50 ± 0.06	20.48 ± 0.02	20.06 ± 0.04	19.41 ± 0.05	NOT
20190606	58640.85	88.06	–	–	–	–	20.45 ± 0.15	–	–	GTC
20190611	58645.89	92.97	–	–	–	22.01 ± 0.07	20.97 ± 0.03	20.51 ± 0.06	19.90 ± 0.10	NOT
20190619	58653.89	100.76	–	–	–	>21.86	21.40 ± 0.04	20.92 ± 0.10	20.160.10	NOT
20190622	58656.89	103.68	–	–	–	>21.68	20.95 ± 0.10	–	–	WHT

Notes. *Rest-frame phase in days from explosion, MJD = 58550.44 ± 4.
‡Telescope code: LCOGT: Las Cumbres Observatory; LT: 2.0-m Liverpool Telescope: NOT: Nordic Optical Telescope; GTC: Gran Telescopio Canarias; WHT: William Herschel Telescope.
⋆Observation performed in the *U* band.
UBV photometry is in the Vega system, while *ugriz* photometry is in the AB system.

Table A3. *JHK* Vega photometry of SN 2019cad obtained with NOTCam.

UT date	MJD	Phase (d)*	*J* (mag)	*H* (mag)	*K* (mag)
20190430	58603.95	52.12	17.29 ± 0.08	16.20 ± 0.10	16.35 ± 0.22
20190521	58624.89	72.51	18.00 ± 0.11	17.26 ± 0.24	17.74 ± 0.32
20190613	58647.89	94.92	20.09 ± 0.13	18.40 ± 0.15	18.24 ± 0.36

Notes. *Rest-frame phase in days from explosion, MJD = 58550.44 ± 4.

Table A4. UV photometry obtained with *Swift* in the AB system.

UT date	MJD	Phase (d)*	UVW2 (mag)	UVM2 (mag)	UVW1 (mag)	U (mag)	B (mag)	V (mag)
20190507	58611.14	59.12	>18.72	>18.84	>18.93	>18.54	>18.50	>17.78

Note. *Rest-frame phase in days from explosion, MJD = 58550.44 ± 4.

[1]*Finnish Centre for Astronomy with ESO (FINCA), University of Turku, FI-20014 Turku, Finland*
[2]*Tuorla Observatory, Department of Physics and Astronomy, University of Turku, FI-20014 Turku, Finland*
[3]*Department of Physics and Astronomy, University of Southampton, Southampton SO17 1BJ, UK*
[4]*Facultad de Ciencias Astronómicas y Geofísicas, Universidad Nacional de La Plata, Paseo del Bosque S/N, B1900FWA La Plata, Argentina*
[5]*Instituto de Astrofísica de La Plata (IALP), CCT-CONICET-UNLP. Paseo del Bosque S/N, B1900FWA La Plata, Argentina*
[6]*Kavli Institute for the Physics and Mathematics of the Universe (WPI), The University of Tokyo, 5-1-5 Kashiwanoha, Kashiwa, Chiba 277-8583, Japan*
[7]*Universidad Nacional de Río Negro. Sede Andina, Mitre 630 (8400), Bariloche, Argentina*
[8]*Consejo Nacional de Investigaciones Científicas y Tecnicas (CONICET), Argentina*
[9]*INAF - Osservatorio Astronomico di Padova, Vicolo dell'Osservatorio 5, I-35122 Padova, Italy*
[10]*Departamento de Ciencias Fisicas, Universidad Andres Bello, Avda. Republica 252, Santiago, Chile*

Table A5. ZTF AB optical photometry.

UT date	MJD	Phase (d)*	Band	Magnitude (mag)
20190314	58556.20	5.61	*r*	>19.61
20190316	58558.20	7.56	*r*	>19.18
20190317	58559.24	8.57	*r*	19.02 ± 0.11
20190317	58559.30	8.63	*g*	19.31 ± 0.24
20190320	58562.15	11.41	*r*	18.75 ± 0.14
20190320	58562.24	11.49	*g*	>18.54
20190325	58567.20	16.32	*g*	19.73 ± 0.18
20190325	58567.22	16.34	*r*	18.67 ± 0.09
20190330	58572.20	21.19	*g*	20.16 ± 0.24
20190330	58572.22	21.21	*r*	18.83 ± 0.15
20190402	58575.21	24.13	*r*	18.95 ± 0.13
20190402	58575.26	24.17	*g*	20.09 ± 0.23
20190407	58580.21	29.00	*r*	19.08 ± 0.11
20190409	58582.20	30.93	*r*	18.76 ± 0.08
20190411	58584.22	32.90	*g*	19.09 ± 0.12
20190414	58587.21	35.81	*g*	18.21 ± 0.06
20190416	58589.22	37.77	*r*	17.50 ± 0.05
20190418	58591.34	39.84	*r*	17.39 ± 0.05
20190420	58593.33	41.77	*r*	17.37 ± 0.06
20190421	58594.16	42.58	*r*	17.41 ± 0.03
20190421	58594.18	42.60	*g*	17.68 ± 0.05
20190425	58598.20	46.52	*g*	17.79 ± 0.05
20190426	58599.15	47.44	*r*	17.49 ± 0.05
20190428	58601.26	49.50	*r*	17.65 ± 0.05
20190502	58605.22	53.36	*g*	18.58 ± 0.08
20190505	58608.19	56.25	*g*	18.94 ± 0.10
20190514	58617.19	65.01	*g*	19.79 ± 0.17
20190514	58617.22	65.04	*r*	18.99 ± 0.11
20190515	58618.26	66.06	*r*	19.30 ± 0.20

Note. *Rest-frame phase in days from explosion, MJD = 58550.44 ± 4.

[11]*Millennium Institute of Astrophysics (MAS), Nuncio Monseñor Sotero Sanz 100, Providencia, Santiago, Chile*
[12]*European Southern Observatory, Alonso de Córdova 3107, Casilla 19, Santiago, Chile*
[13]*Astrophysics Research Centre, School of Mathematics and Physics, Queens University Belfast, Belfast BT7 1NN, UK*
[14]*DTU Space, National Space Institute, Technical University of Denmark, Elektrovej 327, DK-2800 Kgs. Lyngby, Denmark*
[15]*School of Physics & Astronomy, Cardiff University, Queens Buildings, The Parade, Cardiff CF243AA, UK*
[16]*Institute of Space Sciences (ICE, CSIC), Campus UAB, Carrer de Can Magrans s/n, E-08193 Barcelona, Spain*
[17]*School of Physics, O'Brien Centre for Science North, University College Dublin, Belfield, Dublin 4, Dublin, Ireland*
[18]*Department of Physics and Astronomy, Aarhus University, Ny Munkegade, DK-8000 Aarhus C, Denmark*
[19]*Department of Physics, University of California, Santa Barbara, CA 93106-9530, USA*
[20]*Las Cumbres Observatory, 6740 Cortona Dr, Suite 102, Goleta, CA 93117-5575, USA*
[21]*Institute of Cosmology and Gravitation, University of Portsmouth, Portsmouth PO1 3FX, UK*
[22]*Departamento de Física Teórica y del Cosmos, Universidad de Granada, E-18071 Granada, Spain*
[23]*Université de Lyon, Lyon, France; Université de Lyon 1, Villeurbanne; CNRS/IN2P3, Institut de Physique des Deux Infinis, F-69622 Lyon, France*

Table A6. Spectroscopic observations of SN 2019cad.

UT date	MJD	Phase (d)*	Range (Å)	Telescope + Instrument	Grism/Grating
20190322	58564.36	13.56	3500–10 000	LCOGT + FLOYDS	red/blue
20190325	58567.95	17.51	3780–9200	P60 + SEDM	
20190327	58569.32	18.39	3500–9250	LCOGT + FLOYDS	red/blue
20190401	58573.38	22.34	3500–10 000	LCOGT + FLOYDS	red/blue
20190419	58592.02	40.50	4020–7990	LT + SPRAT	VPH
20190420	58593.95	42.38	4020–7990	LT + SPRAT	VPH
20190423	58596.87	45.22	3600–9180	NOT + ALFOSC	Grism#4
20190428	58601.91	50.13	3420–9690	NOT + ALFOSC	Grism#4
20190501	58604.94	53.08	3500–9590	NOT + ALFOSC	Grism#4
20190511	58614.90	62.78	3500–9690	NOT + ALFOSC	Grism#4
20190516	58619.92	67.67	3500–9650	NOT + ALFOSC	Grism#4
20190606	58640.93	88.14	4000–10 235	GTC + OSIRIS	R1000B + R1000R

Note. *Rest-frame phase in days from explosion, MJD = 58550.44 ± 4. **Telescope code:** LCOGT: Las Cumbres Observatory; P60: 60-in Telescope; LT: 2.0-m Liverpool Telescope; NOT: Nordic Optical Telescope; GTC: Gran Telescopio Canarias.

This paper has been typeset from a TEX/LATEX file prepared by the author.